

JPL Publication 95-1, Vol. 2

Summaries of the Fifth Annual JPL Airborne Earth Science Workshop January 23–26, 1995

Volume 2. TIMS Workshop

Vincent J. Realmuto
Editor

January 23, 1995

NASA

National Aeronautics and
Space Administration

Jet Propulsion Laboratory
California Institute of Technology
Pasadena, California

This publication was prepared by the Jet Propulsion Laboratory, California Institute of Technology, under a contract with the National Aeronautics and Space Administration.

Reference herein to any specific commercial product, process, or service by trade name, trademark, manufacturer or otherwise, does not constitute or imply its endorsement by the United States Government or the Jet Propulsion Laboratory, California Institute of Technology.

ABSTRACT

This publication contains the summaries for the Fifth Annual JPL Airborne Earth Science Workshop, held in Pasadena, California, on January 23–26, 1995. The main workshop is divided into three smaller workshops as follows:

- The Airborne Visible/Infrared Imaging Spectrometer (AVIRIS) workshop, on January 23–24. The summaries for this workshop appear in Volume 1.
- The Airborne Synthetic Aperture Radar (AIRSAR) workshop, on January 25–26. The summaries for this workshop appear in Volume 3.
- The Thermal Infrared Multispectral Scanner (TIMS) workshop, on January 26. The summaries for this workshop appear in Volume 2.

FOREWORD

In one of the papers for the TIMS Workshop, reference is made to a color slide. This slide was supplied at the time of the initial distribution of this volume.

Volume 1: AVIRIS Workshop

High Spectral Resolution Remote Sensing of Canopy Chemistry	1
<i>John D. Aber and Mary E. Martin</i>	
MODTRAN3: An Update and Recent Validations Against Airborne High Resolution Interferometer Measurements	5
<i>Gail P. Anderson, Jinxue Wang, and James H. Chetwynd</i>	
Characteristics of the HYDICE Sensor	9
<i>R. W. Basedow and E. Zalewski</i>	
Quantitative Remote Sensing of Ammonium Minerals, Cedar Mountains, Esmeralda County, Nevada	11
<i>William M. Baugh and Fred A. Kruse</i>	
CNR LARA Project, Italy: Airborne Laboratory for Environmental Research	15
<i>R. Bianchi, R. M. Cavalli, L. Fiumi, C. M. Marino, and S. Pignatti</i>	
Using Dark Current Data to Estimate AVIRIS Noise Covariance and Improve Spectral Analyses	19
<i>Joseph W. Boardman</i>	
Mapping Target Signatures Via Partial Unmixing of AVIRIS Data	23
<i>Joseph W. Boardman, Fred A. Kruse, and Robert O. Green</i>	
Combined Hyperspatial and Hyperspectral Imaging Spectrometer Concept	27
<i>Ian Burke and Harold Zwick</i>	
Airborne Visible/Infrared Imaging Spectrometer (AVIRIS) Onboard Calibration System	31
<i>Thomas G. Chrien, Mike Eastwood, Robert O. Green, Charles Sarture, Howell Johnson, Chris Chovit, and Pavel Hajek</i>	
New Calibration Techniques for the Airborne Visible/Infrared Imaging Spectrometer (AVIRIS)	33
<i>Thomas G. Chrien, Robert O. Green, Chris Chovit, Mike Eastwood, Jessica Faust, Pavel Hajek, Howell Johnson, H. Ian Novack, and Charles Sarture</i>	
Initial Vegetation Species and Senescence/Stress Indicator Mapping in the San Luis Valley, Colorado, Using Imaging Spectrometer Data	35
<i>Roger N. Clark, Trude V. V. King, Cathy Ager, and Gregg A. Swayze</i>	

Mapping Minerals, Amorphous Materials, Environmental Materials, Vegetation, Water, Ice and Snow, and Other Materials: The USGS Tricorder Algorithm	39
<i>Roger N. Clark and Gregg A. Swayze</i>	
Calibration to Surface Reflectance of Terrestrial Imaging Spectrometry Data: Comparison of Methods	41
<i>Roger N. Clark, Gregg A. Swayze, Kathy Heidebrecht, Robert O. Green, and Alexander F. H. Goetz</i>	
Causal Correlation of Foliar Biochemical Concentrations With AVIRIS Spectra Using Forced Entry Linear Regression	43
<i>Terence P. Dawson, Paul J. Curran, and John A. Kupiec</i>	
Mineralogic Variations in Fluvial Sediments Contaminated by Mine Tailings as Determined From AVIRIS Data, Coeur d'Alene River Valley, Idaho	47
<i>W. H. Farrand and Joseph C. Harsanyi</i>	
A Layered Approach to Technology Transfer of AVIRIS Between Earth Search Sciences, Inc., and the Idaho National Engineering Laboratory	51
<i>James S. Ferguson, JoAnne E. Ferguson, John Peel, III, and Larry Vance</i>	
Evaluation of the Photochemical Reflectance Index in AVIRIS Imagery	55
<i>John A. Gamon, Dar A. Roberts, and Robert O. Green</i>	
Correction of Thin Cirrus Effects in AVIRIS Images Using the Sensitive 1.375- μ m Cirrus Detecting Channel	59
<i>Bo-Cai Gao and Yoram J. Kaufman</i>	
Remote Sensing of Smoke, Clouds, and Radiation Using AVIRIS During SCAR Experiments	63
<i>Bo-Cai Gao, Lorraine Remer, and Yoram J. Kaufman</i>	
High Accuracy In-Flight Wavelength Calibration of Imaging Spectrometry Data	67
<i>Alexander F. H. Goetz, Kathleen B. Heidebrecht, and Thomas G. Chrien</i>	
Determination of the In-Flight Spectral Calibration of AVIRIS Using Atmospheric Absorption Features	71
<i>Robert O. Green</i>	
An Improved Spectral Calibration Requirement for AVIRIS	75
<i>Robert O. Green</i>	

Movement of Water Vapor in the Atmosphere Measured by an Imaging Spectrometer at Rogers Dry Lake, CA	79
<i>Robert O. Green and James E. Conel</i>	
In-Flight Radiometric Calibration of AVIRIS in 1994	83
<i>Robert O. Green, James E. Conel, Mark Helmlinger, Jeannette van den Bosch, and Pavel Hajek</i>	
Measurement of Atmospheric Water Vapor, Leaf Liquid Water and Reflectance With AVIRIS in the Boreal Ecosystem-Atmosphere Study: Initial Results	87
<i>Robert O. Green, James E. Conel, and Dar A. Roberts</i>	
Measurement of the Spectral Absorption of Liquid Water in Melting Snow With an Imaging Spectrometer	91
<i>Robert O. Green and Jeff Dozier</i>	
Vegetation Species Composition and Canopy Architecture Information Expressed in Leaf Water Absorption Measured in the 1000 nm and 2200 nm Spectral Region by an Imaging Spectrometer	95
<i>Robert O. Green and Dar A. Roberts</i>	
Prospect Redux	99
<i>S. Jacquemoud, S. L. Ustin, J. Verdebout, G. Schmuck, G. Andreoli, and B. Hosgood</i>	
AVIRIS User's Guide	105
<i>Howell K. Johnson and Robert O. Green</i>	
Integration of AIRSAR and AVIRIS Data for Trail Canyon Alluvial Fan, Death Valley, California	109
<i>Kathryn S. Kierein-Young</i>	
Remote Mineral Mapping Using AVIRIS Data at Summitville, Colorado, and the Adjacent San Juan Mountains	113
<i>Trude V. V. King, Roger N. Clark, Cathy Ager, and Gregg A. Swayze</i>	
Aircraft Scanner Data Availability Via the Version 0 Information Management System	117
<i>G. R. Mah</i>	
An Algorithm for Chlorophyll Using First Difference Transformations of AVIRIS Reflectance Spectra	121
<i>Evelyn Novo, Mary Gastil, and John Melack</i>	

Improving Alpine-Region Spectral Unmixing With Optimal-Fit Snow Endmembers	125
<i>Thomas H. Painter, Dar A. Roberts, Robert O. Green, and Jeff Dozier</i>	
Using Foreground/Background Analysis to Determine Leaf and Canopy Chemistry	129
<i>J. E. Pinzon, S. L. Ustin, Q. J. Hart, S. Jacquemoud, and M. O. Smith</i>	
AVIRIS Spectral Trajectories for Forested Areas of the Gifford Pinchot National Forest	133
<i>Donald E. Sabol, Jr., Milton O. Smith, John B. Adams, Janet H. Zakin, Compton J. Tucker, Dar A. Roberts, and Alan R. Gillespie</i>	
Sub-Pixel Localization of Highways in AVIRIS Images	137
<i>Yehuda Salu</i>	
Validating Spatial Structure in Canopy Water Content Using Geostatistics	141
<i>E. W. Sanderson, M. H. Zhang, S. L. Ustin, E. Rejmankova, and R. S. Haxo</i>	
Airborne Visible/Infrared Imaging Spectrometer (AVIRIS): Sensor Improvements for 1994 and 1995	145
<i>C. M. Sarture, T. G. Chrien, R. O. Green, M. L. Eastwood, H. K. Johnson, C. J. Chovit, P. Hajek, J. L. Holbrook, J. J. Raney, and M. A. Hernandez</i>	
Extraction of Ozone and Chlorophyll-A Distribution From AVIRIS Data . . .	149
<i>M. Schaepman, K. I. Itten, D. Schläpfer, U. Kurer, S. Veraguth, and J. Keller</i>	
Impact of Differences in the Solar Irradiance Spectrum on Surface Reflectance Retrieval With Different Radiative Transfer Codes	153
<i>K. Staenz, D. J. Williams, G. Fedosejevs, and P. M. Teillet</i>	
Spectral Identification of Minerals Using Imaging Spectrometry Data: Evaluating the Effects of Signal to Noise and Spectral Resolution Using the Tricorder Algorithm	157
<i>Gregg A. Swayze and Roger N. Clark</i>	
Preliminary Study of Kelso Dunes Using AVIRIS, TM, and AIRSAR	159
<i>Pung Xu, Dan G. Blumberg, and Ronald Greeley</i>	

Volume 2: TIMS Workshop

Analyses of TIMS and AVIRIS Data, Integrated with Field and Laboratory Spectra, for Lithological and Mineralogical Interpretation of Vulcano Island, Italy	1
<i>M. Fabrizia Buongiorno, M. Paola Bogliolo, Stefano Salvi, David C. Pieri, and Francesco Geneselli</i>	
Urban Remote Sensing Applications: TIMS Observations of the City of Scottsdale	5
<i>Philip R. Christensen, David E. Melendrez, Donald L. Anderson, Victoria E. Hamilton, Melissa L. Wenrich, and Douglas Howard</i>	
For Geologic Investigations With Airborne Thermal Infrared Multispectral Images: Transfer of Calibration From Laboratory Spectrometer to TIMS as Alternative for Removing Atmospheric Effects	9
<i>Kenneth S. Edgett and Donald L. Anderson</i>	
Aeolian Erosion, Transport, and Deposition of Volcaniclastic Sands Among the Shifting Sand Dunes, Christmas Lake Valley, Oregon: TIMS Image Analysis	13
<i>Kenneth S. Edgett, Michael S. Ramsey, and Philip R. Christensen</i>	
The JPL Field Emission Spectrometer	17
<i>Simon J. Hook and Anne B. Kahle</i>	
"A Conflict of Water and Fire": Remote Sensing Imagery of the Uinkaret Volcanic Field, Grand Canyon, Arizona	19
<i>Michael S. Ramsey</i>	
The 1994 Laboratory Calibration of TIMS	25
<i>Vincent J. Realmuto, Pavel Hajek, Mahadeva P. Sinha, and Thomas G. Chrien</i>	
The 1994 TIMS Airborne Calibration Experiment: Castaic Lake, California	29
<i>Vincent J. Realmuto, Simon J. Hook, and Jeannette van den Bosch</i>	
Discrimination of Alkalinity in Granitoid Rocks: A Potential TIMS Application	33
<i>Steven W. Ruff</i>	
TIMS Observations of Surface Emissivity in HAPEX-Sahel	37
<i>Thomas Schmugge, Simon Hook, and Anne Kahle</i>	
A Field- and Laboratory-Based Quantitative Analysis of Alluvium: Relating Analytical Results to TIMS Data	39
<i>Melissa L. Wenrich, Victoria E. Hamilton, and Philip R. Christensen</i>	

Volume 3: AIRSAR Workshop

New Observations of Bolivian Wind Streaks by JPL Airborne SAR; Preliminary Results	1
<i>Dan G. Blumberg and Ronald Greeley</i>	
Measuring Soil Moisture with Imaging Radars	5
<i>Pascale C. Dubois, Jakob van Zyl and Ted Engman</i>	
Use of TOPSAR Digital Elevation Data to Determine the 3-Dimensional Shape of an Alluvial Fan	9
<i>Tom G. Farr</i>	
Accurate Estimation of σ^0 Using AIRSAR Data	13
<i>Francesco Holecz and Eric Rignot</i>	
Remotely Sensed Indicators of Habitat Heterogeneity and Biological Diversity: A Preliminary Report	17
<i>Marc Imhoff, Thomas Sisk, Anthony Milne, Garth Morgan, and Tony Orr</i>	
Polarization and Wavelength Diversities of Gulf Stream Fronts Imaged by AIRSAR	21
<i>J. S. Lee, R. W. Jansen, G. O. Marmorino, and S. R. Chubb</i>	
Bayes Classification of Interferometric TOPSAR Data	25
<i>T. R. Michel, E. Rodriguez, B. Houshmand, and R. Carande</i>	
Terrain Classification Using Circular Polarimetric Features	27
<i>David G. Michelson, Ian G. Cumming, and Charles E. Livingstone</i>	
Use of AIRSAR to Identify Woody Shrub Invasion and Other Indicators of Desertification in the Jornada LTER	31
<i>H. Brad Musick, Gerald G. Schaber, and Carol S. Breed</i>	
The Unique Radar Scattering Properties of Silicic Lava Flows and Domes	35
<i>Jeffrey J. Plaut, Ellen R. Stofan, Steven W. Anderson, and David A. Crown</i>	
On the Potential of Long Wavelength Imaging Radars for Mapping Vegetation Types and Woody Biomass in Tropical Rain Forests	39
<i>Eric J. Rignot, Reiner Zimmermann, and Ram Oren</i>	
Lithologic Controls on AIRSAR Signatures of Bedrock and Alluvium, at Lunar Crater, Nevada	43
<i>Benoit Rivard, Marc D'Iorio, and Paul Budkewitsch</i>	

Estimation of Penetration of Forest Canopies by Interferometric SAR Measurements	47
<i>Ernesto Rodriguez, Thierry R. Michel, and David J. Harding</i>	
Regional Mapping of Forest Canopy Water Content and Biomass Using AIRSAR Images Over BOREAS Study Area	49
<i>Sasan Saatchi, Eric Rignot, and Jakob van Zyl</i>	
Application of IEM Model on Soil Moisture and Surface Roughness Estimation	51
<i>Jiancheng Shi, J. R. Wang, P. E. O'Neill, A. Y. Hsu, and E. T. Engman</i>	



Analyses of TIMS and AVIRIS Data, Integrated with Field and Laboratory Spectra, for Lithological and Mineralogical Interpretation of Vulcano Island, Italy

M. Fabrizia Buongiorno¹, M. Paola Bogliolo¹, Stefano Salvi¹, David C. Pieri², and Francesco Geneselli¹

¹ Istituto Nazionale di Geofisica, Via di Vigna Murata 605, Roma 00143, Italy

² Jet Propulsion Laboratory, California Institute of Technology, 4800 Oak Grove Dr., Pasadena, CA 91109

1. Introduction

Vulcano Island is part of the Eolian archipelago, located about 25 km from the north-east coast of Sicily. The archipelago comprises seven major volcanic islands, two of which are active volcanoes (Vulcano and Stromboli). Vulcano covers an area of about 50 km², and is about 10 km long.

The volcanic history of the island is spanned by its four main structural units: (I) the South Vulcano complex (stratovolcano) and the Piano Caldera, (II) the Lentia Group, (III) the Fossa Caldera and Fossa Vulcano complex, and (IV) Vulcanello, which is connected to the main Vulcano Island by a half-kilometer-wide isthmus; see Figure 1. The oldest structure, the South Vulcano, probably originated in the upper Pleistocene. The youngest structure, Vulcanello, originated in an eruption that occurred about 183 B.C. The volcanic rock types found on Vulcano range from mafic to intermediate-acidic in composition.

Explosive volcanic activity has predominated in the geological evolution of Vulcano Island, and there is no evidence that this pattern has ceased. Rather, the current situation is one of unrest, so a strict regimen of continuous geophysical and geochemical monitoring has been undertaken over the last decade. Though the year-round population of Vulcano is small (under 1000), during the summer the island becomes a very popular resort, and has thousands of additional tourists at any time throughout the high season, thus substantially increasing the number of people potentially at risk from an explosive eruption or other hazards such as noxious gas emissions (e.g., CO₂, H₂S, SO₂).

During the past ten years, remote sensing data have been repetitively acquired with optical and microwave airborne sensors (see Table 1). The present work shows the preliminary results of a study based on the integration of various remote sensing data sets with field spectroscopy, and other laboratory analyses, for the geological and geomorphological mapping of the island. It is hoped that such work will also usefully contribute to the evaluation of the volcanic hazard potential of the island, as well as to the evaluation of the status of its current activity.

2. Image Data

The remote sensing imagery available for Vulcano is tabulated here in Table 1. Our study utilized data from airborne optical sensors operating in the very-near (VNIR), short-wave (SWIR) and thermal (TIR) parts of the infrared spectrum. The TIR data used here were acquired in 1986 during C-130 aircraft overflights with the Thermal Infrared Multispectral Scanner (TIMS: 8-12 μm, 6 channels) as part of a JPL/NASA-CNR airborne campaign over volcanoes in southern Italy (Bianchi *et al.*, 1990). Although Thematic Mapper Simulator (NS001) data were also acquired during that campaign, we preferred to use the more comprehensive VNIR-SWIR data set acquired with the Airborne Visible/Infrared Imaging Spectrometer (AVIRIS: 0.4-2.5 μm, 224 channels) taken during the subsequent NASA-CNR MAC-EUROPE '91 ER-2 deployment. Aircraft for these campaigns were deployed by the Medium and High Altitude Missions groups of NASA Ames Research Center in Palo Alto, California.

3. Other Data Sets

Ground truth information in the VNIR-SWIR was collected by performing field measurements with a portable spectro-radiometer (GER Mark IV) at different times, but

Table 1.

Multispectral Airborne Sensor Data Acquired Over Vulcano Island

<i>Sensor</i>	<i>Flight Date</i>	<i>Sensor</i>	<i>Flight Date</i>
TIMS	29 July 1986	AIRSAR	28 June 1991
NS001	29 July 1986	MIVIS	21 July 1994
AVIRIS	19 July 1991	TMS	19 July 1991

in the same season as the image data acquisition. Rock samples were collected for spectral analyses in the TIR wavelengths, since a portable spectrometer was not available for this spectral range.

A digital elevation model (DEM) was created by digitizing a topographic map at the 1:10,000 scale (courtesy AGIP Oil Corporation, 1980), with vector interpolation of the contour lines. The DEM was used for both geometric rectification of the remotely sensed images (e.g., TIMS, AVIRIS) and for morphological and structural interpretations.

Rock samples were collected on the most representative volcanic formations and were spectrally and chemically analyzed for information regarding mineralogical composition.

4. Atmospheric Correction of TIMS and AVIRIS Data

Calibrated AVIRIS radiance data were corrected for atmospheric effects by using LOWTRAN-7 and MODTRAN radiative transfer models (Berk *et al.*, 1989). As input for the models, we used atmospheric profiles and ground reflectance measurements performed over a flat field reference. TIMS data were also corrected for atmospheric effects by using radiative transfer models (LOWTRAN-7). Spectral emissivity was then calculated by using a normalization technique (Realmuto, 1990).

5. Analysis Approach

Reflectance and emissivity image data were analyzed--first separately and then combined in color composites--for geological and lithological interpretation by means of photo-interpretation techniques. A comparison of the retrieved emissivity and reflectance values was performed by extracting image spectra relative to the surface materials for which we had also made field and laboratory measurements. The AVIRIS reflectance images were analyzed by means of principal component techniques (Gillespie *et al.*, 1986) in order to compress the data dimension but retain the spectral information of the selected channels. The most significant color composites of the principal component analyses were then co-registered with the DEM for the combined analysis with TIMS images. TIMS emissivity images were analyzed using decorrelation stretching techniques.

6. Preliminary Results

The preliminary results showed that it is possible to compare the TIMS-retrieved emissivity spectra (Figure 2) with the laboratory ones for the well-exposed volcanic materials (Figure 3). The analysis of mixed AVIRIS reflectance and TIMS emissivity image color composites showed color variations that are in good agreement with changes in the surficial lithologic composition of the various volcanic products. Observed variations of the surface roughness of the exposed volcanics at the 1-100 cm scale also play a role in increasing the variance of the spectral response.

7. Future Work

The next step is to complete the comparison between laboratory spectra in the

VNIR-SWIR range with AVIRIS-retrieved reflectance spectra. Additionally, microwave image data acquired by the JPL-AIRSAR during the MAC-EUROPE '91 campaign will be integrated with the optical data to add necessary textural information.

During the summer of 1994, the new Multispectral Infrared and Visible Imaging Spectrometer (MIVIS) of the Italian National Research Council (CNR), under the auspices of the Project for Environmental Studies of Southern Italy (LARA), was also flown over the Eolian Islands. Multi-temporal images were acquired in both the VNIR-SWIR and TIR bandpasses, and a detailed ground measurement campaign was carried out during the overflights. The future analyses and interpretation of these data will hopefully increase the accuracy of the lithologic mapping and hazard assessment not only on Vulcano Island, but on other more complex areas, such as Mt. Etna, where some of us are also attempting to apply these techniques to address geological and hazard-related problems.

8. Acknowledgements

Work described in this paper was completed, in part, at the Istituto Nazionale di Geofisica di Italy under funding from the Italian government, and at the Jet Propulsion Laboratory, California Institute of Technology, under contract with NASA.

9. Bibliography

- Bianchi, R., R. Casacchia, A. Coradini, A.M. Duncan, J.E. Guest, A. Kahle, P. Lanciano, D.C. Pieri, and M. Poscolieri, 1990, Remote sensing of Italian volcanoes, *EOS Trans., AGU*, 71, 1789-1791.
- Berk, A., L.S. Bernstein and D.C. Robertson, 1989, *MODTRAN: A moderate resolution model for LOWTRAN7*, *GL-TR-0122*, AFGL, Hanscom Air Force Base, Bedford, MA 01731.
- Gillespie, A.R., A.B. Kahle, and R.E. Walker, 1986, Color enhancements of highly correlated images: I. Decorrelation and HSI contrast stretches, *Remote Sensing of the Environment*, 20, 209-235.
- Realmuto, V.J., 1990, Separating the Effects of Temperature and Emissivity: Emissivity Spectrum Normalization, *Proc. Second Thermal Infrared Multispectral Scanner Workshop, Publ. 90-55*, JPL, Pasadena, CA 91109.

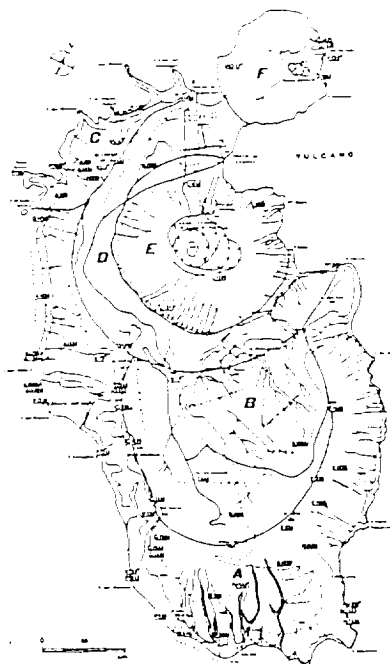


Figure 1.

The main geological and structural units of Vulcano Island:

(A) and (B)--South Volcano and Piano Caldera

(C)--the Lentia Group (latite, trachyte, and rhyolite lava dome complex):

(D) and (E)--Fossa Caldera and Fossa Volcano;

(F)--Vulcanello

**ORIGINAL PAGE IS
OF POOR QUALITY**

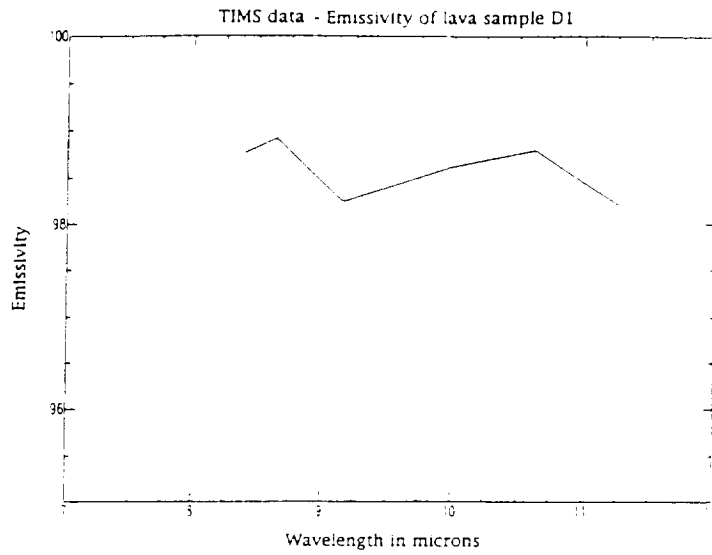


Figure 2.
Emissivity of a Lentia lava flow retrieved from TIMS data versus wavelength.

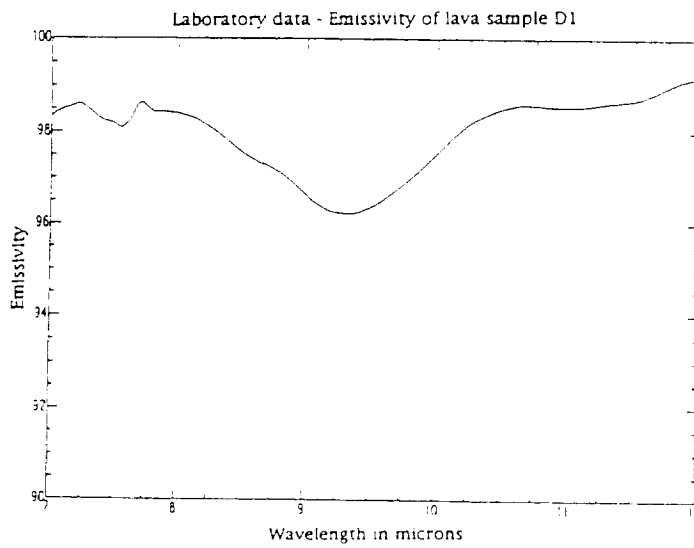


Figure 3.
Emissivity of a sample of a Lentia lava flow measured in the laboratory versus wavelength.

URBAN REMOTE SENSING APPLICATIONS: TIMS OBSERVATIONS OF THE CITY OF SCOTTSDALE

Philip R. Christensen, David E. Melendrez, Donald L. Anderson, Victoria E. Hamilton, Melissa L. Wenrich, and Douglas Howard

Department of Geology
Arizona State University
Tempe, AZ 85287-1404

1. INTRODUCTION

A research program has been initiated between Arizona State University and the City of Scottsdale, Arizona to study the potential applications of TIMS data for urban scene classification, desert environmental assessment, and change detection. This program is part of a long-term effort to integrate remote sensing observations into state and local planning activities to improve decision making and future planning. Specific test sites include a section of the downtown Scottsdale region that has been mapped in very high detail as part of a pilot program to develop an extensive GIS database. This area thus provides excellent "ground truth" for surface classification models and contains an excellent time history of the evolution of the city infrastructure, such as the timing and composition of street repavement. A second area of study includes the McDowell Mountains immediately east of the city. These mountains are currently undergoing intensive study by state and local agencies to assess potential sites for urban development as well as preservation. These activities are of particular relevance as the Phoenix metropolitan area undergoes major expansion into the surrounding desert area.

The objectives of this study in urban areas are aimed at determining potential applications of TIMS data for classifying and assessing land use and surface temperatures. Land use centers on surface impermeability studies for storm runoff assessment and pollution control. These studies focus on determining the areal abundance of urban materials such as pavement, concrete, building footprints, and pools versus urban vegetation and undeveloped soil. Highly experimental applications include assessment and monitoring of pavement condition. Temperature studies focus on determining swimming pool area and temperature for use in monitoring evaporation and urban water consumption. These data will also be used to determine building and ground temperatures for assessing changes in the urban environment.

The desert terrain mapping aspect of this study is aimed at combining soil and rock composition and vegetation studies with digital terrain models to aid in the identification and preservation of unique desert environments. Derived products and applications will include the overlay of TIMS-derived compositional classifications on ~1 foot horizontal and vertical resolution Digital Elevation Model data acquired by the City of Scottsdale for input into flood runoff predictive models. The TIMS data will also be combined with NS001 data acquired simultaneously by the C130 aircraft and 6 inch resolution air digital orthographic color images acquired by the City of Scottsdale for scene classification.

The TIMS data were collected by the Ames C130 aircraft on August 18, 1994, with three image lines over the central urban region of Scottsdale and six covering the McDowell Mountains. The Scottsdale images were taken at an average altitude of 4900 feet (AGL) and have a calculated scale of about 12.2 feet/pixel (3.7 m/pixel) (assuming 2.5 mrad IFOV). We estimate the actual spatial resolution to be about 13-16 feet (~4-5 meters). Over the McDowells, the surface elevation varies by about 3500 feet with respect to the average aircraft altitude of 9400 feet (MSL). Image scale can therefore only be approximated to be about 12.4 ± 3.1 feet/pixel ($\sim 3.8 \pm 1$ m/pixel). The images are 638 samples by 7600-8900 lines in size.

2. SPECTRAL AND GEOMETRIC CALIBRATIONS

The spectral calibration procedures have primarily focused on optimizing the atmospheric water and ozone corrections. We are continuing to investigate the relative affects of both water and ozone on the six-point spectra obtained from the images in both radiance- and emissivity-space. The standard radiometric correction routines within the VICAR software package are being used, one of which runs "lowtran7" as a subroutine.

Because the images were collected over the Phoenix area on a warm Summer morning, it is likely that the atmosphere was relatively dry compared to the standard "northern hemisphere mid-latitude Summer" model used in lowtran. Also, the lack of a detailed atmospheric profile for that day has required a very systematic approach to best determine the correct ozone- and water-factors for use in the calibration.

2.1 Spectral and Temperature Data Extraction

The McDowell images have about a 40-45% cross-track overlap (Figure 1). We have chosen the two westernmost images of the McDowells (hereafter referred to as L8 and L9) for the calibration study. The images L8 and L9 contain a water canal in the area of overlap which can be used for extracting radiance and emissivity spectra and water temperature values at a variety of emission angles and viewing perspectives. For the emissivity calculations, the 8-bit emissivity DN values are stretched to fit a max. and min. emissivity of 0.985 and 0.7, respectively, with band six constrained as the reference band held fixed at the max. emissivity.

Five data points along the water canal are being used consistently throughout: three within the area of overlap and one at the nadir point for each image (Figures 1, 2). The spectral calibrations are work in progress although we are clearly seeing that the spectra are much more sensitive to atmospheric water than ozone. Also, it appears that fractional lowtran water values (0-0.25) are yielding the best results.

2.2 Geometric Corrections

Preliminary spatial warping and geometric corrections have also been performed. A portion of the TIMS image covering the Scottsdale Civic Center was warped to fit a digital street grid. Approximately 120 ground control points were collected between the two images (using the ERDAS Imagine software) which equates to a 13th- or 14th-order polynomial fit. This was done subsequent to the correction for instrument scan distortions in VICAR. The poly-warp was significantly better than the scan mirror correction alone with only minor residual differences from the city grid. Future plans call for all the Scottsdale TIMS images to be rectified to the city grid. The images of the McDowells will eventually be mosaicked and tied to either Landsat or aerial photos of the area in a UTM projection.

3. PRELIMINARY SCENE CLASSIFICATIONS

A major expense for the City of Scottsdale is street maintenance. The ability to classify the pavement condition by remote sensing could potentially save many dollars/man hours. As a test case, a TIMS image covering the downtown section of the City of Scottsdale is being used for classification of urban materials. The scene contains materials such as vegetation (golf course, baseball stadium, lawns), water (ponds, fountains, pools, canals), concrete (sidewalks, medians, parking structures), roofing materials (asphalt/cedar shingles, metal, clay, slate, foam/paint), and street materials (old/new pavement, chip sealing, red brick, dirt, people, vehicles).

The method used for image classification is target transformation principal component analysis (Anderson, 1993). Six point TIMS spectra of known materials directly from the image are used as endmembers. The spectra are transformed into the fourier domain prior

to classification to decorrelate each of the bands. The street boundaries can be masked from the rest of the image for more specific classification using the Scottsdale GIS street easement information. Preliminary results show significant differentiation of many endmembers, including newly paved/sealed versus older asphalt. Future work entails combining the TIMS images with those from NS001 and Scottsdale visible digital color orthographic images for even better material differentiation. Radar images have also been recently acquired which should be useful for surface roughness as a classifier of pavement condition.

4. ACKNOWLEDGMENTS

We wish to express sincere thanks to the entire crew of the Ames C130 aircraft team for the acquisition of the high-quality data used in this study, and for their enthusiasm for our participation in the data collection flights.

5. REFERENCE

Anderson D.L., 1993, Fourier Domain Target Transformation Analysis in the Thermal Infrared (abstract), In *Lunar and Planetary Science XXIV*, Lunar and Planetary Institute, Houston, p. 31.

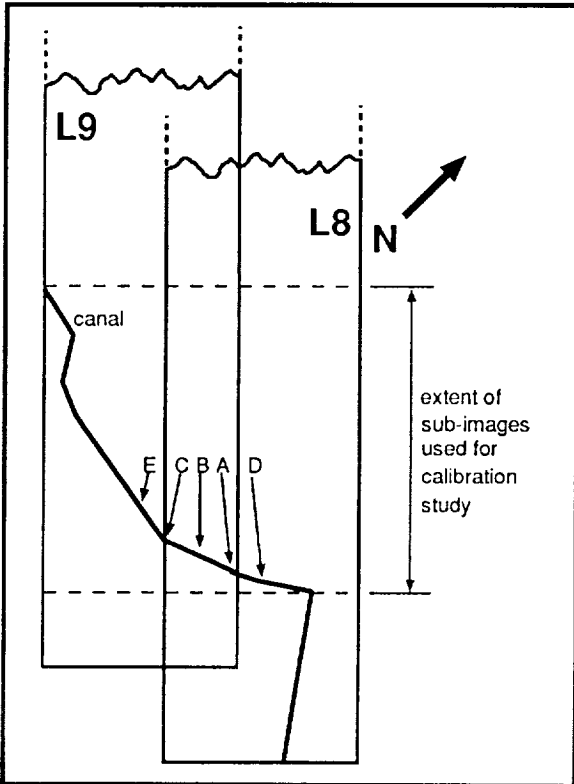


Figure 1. Schematic of TIMS images L8 and L9 covering the western portion of the McDowell Mountains. Data points A-E are being used for extraction of radiance and emissivity spectra as well as temperatures of canal water from various emission angles and viewing perspectives.

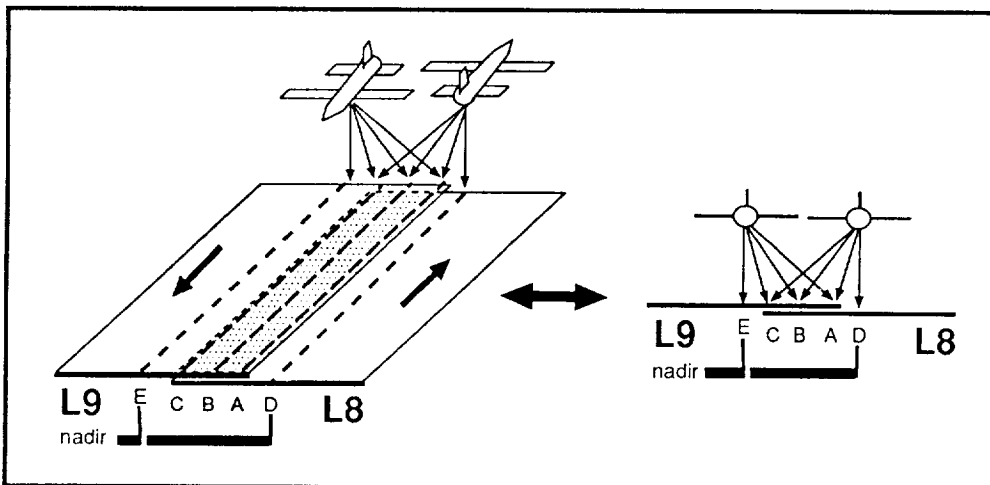


Figure 2. Representations of TIMS images L8 and L9 illustrating viewing angles of data points A-E from adjacent aircraft flight lines. The left diagram shows a perspective view of the flight lines and overlap between images. The right diagram better illustrates the relationship between the viewing and emission angles. Points B have been chosen to be both equidistant (in pixels) and equiangular from nadir.

**FOR GEOLOGIC INVESTIGATIONS WITH AIRBORNE THERMAL
INFRARED MULTISPECTRAL IMAGES: TRANSFER OF CALIBRATION
FROM LABORATORY SPECTROMETER TO TIMS AS ALTERNATIVE FOR
REMOVING ATMOSPHERIC EFFECTS**

Kenneth S. Edgett and Donald L. Anderson

Department of Geology, Arizona State University
Box 871404, Tempe, Arizona, 85287-1404, U.S.A.

1. INTRODUCTION

This paper describes an empirical method to correct TIMS data for atmospheric effects by transferring calibration from a laboratory thermal emission spectrometer to the TIMS multispectral image. The method does so by comparing the laboratory spectra of samples gathered in the field with TIMS 6-point spectra for pixels at the location of field sampling sites. The transference of calibration also makes it possible to use spectra from the laboratory as endmembers in unmixing studies of TIMS data.

2. THE PROBLEM

The emissivity and spectral unmixing study described in this volume by Edgett *et al.* (1995) was designed to use a TIMS image (obtained September 1991) to address the geology of a dune field in Christmas Lake Valley, Oregon. In that study, accurate determination of surface temperature was not required. However, Edgett *et al.* (1995) desired to obtain accurate estimates of surface emissivity, a property directly related to the composition of surface materials. To obtain surface emissivity, the effects of atmospheric contributions (including H₂O vapor in TIMS band 1 and O₃ in band 4) to the TIMS spectrum had to be removed.

Atmospheric correction for TIMS images usually involves the use of a radiative transfer code such as the Lowtran 6 or Lowtran 7 atmospheric models developed for the U.S. Air Force (*e.g.*, see Hook *et al.*, 1994). The Lowtran code uses an input or modeled atmospheric profile. An input profile might include pressure, temperature, and humidity as a function of altitude measured at the time of the TIMS overflight. In the case of most TIMS flights (including that of September 1991 over Christmas Lake Valley), these parameters are usually not measured and a model atmosphere must be assumed. The best model atmosphere that can be assumed by Lowtran for a mid-September overflight in Oregon is for "North American mid-latitude Summer." However, it was found in the Edgett *et al.* (1995) study that the model atmosphere over-predicted the humidity in arid Christmas Lake Valley, Oregon, resulting in radiances for TIMS band 1 that were inordinately higher than in the other five bands. The artificially high radiance in band 1 off-set the emissivities calculated (using the method of Realmuto (1990)) for all six bands, because the surface kinetic temperature is assumed to be the same as that detected by the band with the highest radiance. The main problem that resulted was that band 1 emissivities were exceptionally high relative to the other TIMS bands and to what was observed in laboratory spectra of samples collected from sand dunes located in the TIMS scene (*e.g.*, Figure 1). The problem was the same for spectra of water and vegetation, which should have had relatively flat spectra.

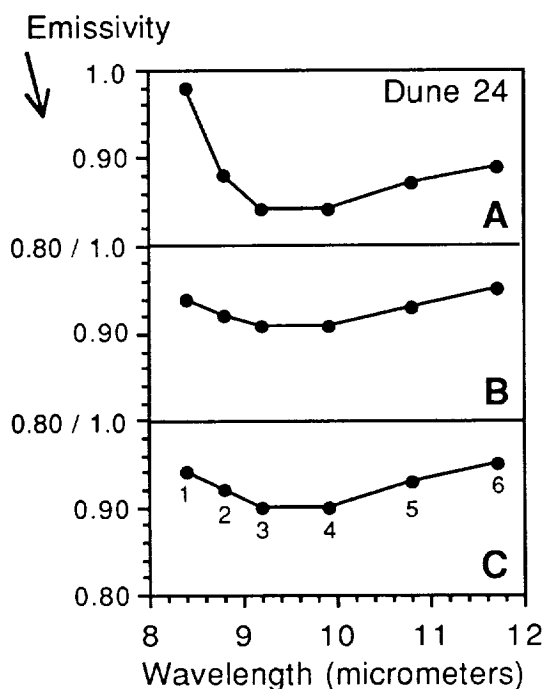


Figure 1. Comparison of six-point emissivity spectra of sand near the crest of one of the dunes in the Shifting Sand Dunes field of Christmas Lake Valley, Oregon (see Edgett *et al.*, 1995). Band 1 through 6 of a TIMS image obtained in September 1991 are indicated. (A) Spectrum from TIMS image using Lowtran atmospheric correction. (B) Spectrum from TIMS image after empirical correction as described here. (C) Laboratory spectrum convolved to TIMS spectral resolution. Note the inordinately high emissivity in band 1 for the Lowtran-corrected spectrum.

3. PROPOSED SOLUTION

When the relative humidity is not known, the atmosphere correction for water vapor can be solved by assuming a different humidity, as suggested by Hook *et al.* (1994). Alternatively, atmospheric effects can be corrected empirically by calibrating the TIMS image to a known surface spectrum, such as a body of water, vegetation, or the spectrum of material collected from the field area. For example, Ondrusek *et al.* (1993) used snow in a TIMS scene to calibrate an image. This approach precludes the need for a radiative transfer code, and therefore might not be easily applied to all thermal infrared images of remote or inaccessible areas, particularly if seen from very high altitudes. However, this alternative approach was used because of (1) the emphasis on surface geology and (2) the difficulty in application of the Lowtran atmospheric model to the Christmas Lake Valley TIMS image of Edgett *et al.* (1995).

Conceptually, the approach followed here is a model for transfer of calibration from the laboratory spectrometer to the TIMS. More sophisticated examples of laboratory spectrometer calibration transfer models are found in papers by Adhietty *et al.* (1991) and Wang and Kowalski (1992). The philosophical justification for this approach is that the atmospheric column during acquisition of laboratory spectra has a very short path length (< 1 m) relative to that of the TIMS in an aircraft (> 3,000 m), and water vapor (humidity) in the laboratory setting is minimal.

Transference of calibration from the laboratory spectrometer data to the TIMS emissivity image requires two main steps. The first is to obtain laboratory spectra of materials that occur within the scene and convolve to TIMS six-band resolution. The second step is to calibrate the TIMS normalized emittance image using the average of several (in this case, 10) of the laboratory spectra and then check the calibration transfer using several other laboratory spectra (here, another 10 were used). The steps followed are described in more detail below.

4. SPECIFIC STEPS

4.1 Laboratory Spectra of Christmas Lake Valley Samples

Laboratory thermal emission spectra of sand samples from the Shifting Sand Dunes of Christmas Lake Valley, Oregon, were obtained, convolved to TIMS six-band resolution, and used in the empirical correction for atmospheric effects (see section 4.2, below). The configuration and calibration of the laboratory thermal emission spectrometer at Arizona State University was described by Christensen and Harrison (1993) and in a manuscript presently being prepared by S.W. Ruff, P.W. Barbera, P.R. Christensen, and D.L. Anderson. Laboratory thermal emission spectra were acquired for this study using a commercial fast Fourier transform infrared spectrometer (Mattson Cygnus, modified for emission measurements) with a spectral resolution of 4 cm^{-1} . Atmospheric contributions to spectra from water and CO_2 are minimized by using a dry nitrogen purge and cold finger to trap excess water. Emission spectra were obtained according to "method 1" of Christensen and Harrison (1993).

Laboratory spectra were collected for 25 bulk sediment samples from the Shifting Sand Dunes. The samples were subsequently impregnated with epoxy and cut for thin section analysis. Twenty of the spectra obtained from the laboratory were used in the procedure for transferring calibration from laboratory data to the TIMS image of the dunes obtained in September 1991. The sand samples contain mostly plagioclase feldspar, volcanic glass, ash aggregates, basalt lithic fragments, pyroxenes, and magnetite/opaque minerals (Edgett, 1994).

4.2 Empirical Transfer of Calibration to TIMS

The empirical corrections for the 1991 TIMS image of the Shifting Sand Dunes of Christmas Lake Valley (see Edgett *et al.*, 1995) involved the following steps:

(1) Normalized emittance (Realmuto, 1990) was derived from the radiance image calibrated to the two onboard blackbodies.

(2) The emittance image was corrected for atmospheric attenuation effects on the sides of the TIMS scan. These effects are caused by the side-scanning nature of TIMS, thus there is more atmosphere between the instrument and surface as a function of angle away from nadir. A low pass filter (1 line by 211 samples) was used to remove high-frequency features. The resulting image was a map of low frequency brightness (in this case, emittance) variations across the image. The image was darker in the middle and brighter on the sides, consistent with increased atmospheric attenuation on the sides of the scan. The average of this brightness variation was then subtracted from the original emittance image, and the result of this step was re-boosted to have the same slope and offset (DN stretch) as the original emittance image.

(3) The average of ten laboratory spectra (convolved to TIMS wavelengths) of samples collected from the field area were compared to the average six-point spectra of the image pixel corresponding to the location where each of the field samples was collected. The average difference between the two data sets were used to correct the emissivity image for atmospheric effects by essentially forcing a transfer of calibration from laboratory to TIMS image. In this case, the average difference in emissivity between the laboratory spectra and TIMS emittance image was 0.007 (bands 1, 2, 5) to 0.027 (band 6).

(4) The newly calibrated and corrected image was checked by comparing ten different (than used in step 3) laboratory spectra to the TIMS image. Again, laboratory spectra are convolved to TIMS six-point resolution and compared with the image emissivity for the pixel corresponding to the site where a sample was collected. The

difference between the two should be small. In this case, differences ≤ 0.01 emissivity were considered to be successful, and the average differences were only 0.001 to 0.003.

5. DISCUSSION AND CONCLUSIONS

In an ideal situation, the spectra used in steps 3 and 4 above should be very different from those of the material of interest in the study. They should also be different from each other (for example, if spectra used in step 3 were for quartzite outcrops and spectra in step 4 were for basalt flows). However, most spectra of samples collected in the vicinity of the Shifting Sand Dunes of Christmas Lake Valley are very similar. There are no outcrops of material composed of something completely different (e.g., quartz-rich rock) relative to the dune sand. All of the geologic materials are glassy volcanics (Edgett, 1994). The spectra that are different from the dune sand are those of materials that typically have relatively flat spectra, like vegetation and fine-grained playa surfaces. The results for step 4 above were compared with the laboratory spectrum of playa salts and indeed found to be flat.

The approach used here to remove atmosphere from a TIMS image appears to be a very promising method for work with airborne thermal infrared images used for geological purposes. The advantage of this approach is that now laboratory spectra can be applied to unmixing analysis of the image. Use of laboratory spectra for mixing analysis means that spectral libraries might be applied with relative ease. Use of laboratory spectra to unmix the September 1991 Shifting Sand Dunes image is a goal of future work (Edgett *et al.*, 1995). Before this is done, however, it will be necessary to further test the empirical atmospheric correction approach by using a different TIMS scene that has surfaces of widely contrasting composition, such as the Kelso - Cima, California image described by Barbera (1989).

6. REFERENCES

- Adhietty, I.S., J.A. McGuire, B. Wangmaneerat, T.M. Niemczyk, and D.M. Haaland, 1991, "Achieving transferable multivariate spectral calibration models: Demonstration with infrared spectra of thin-film dielectrics on silicon," *Analytical Chemistry*, vol. 63, pp. 2329-2338.
- Barbera, P.W., 1989, *The Geology of the Kelso-Baker region, Mohave Desert, California, using Thermal Infrared Multispectral Scanner Data*, M.S. Thesis, Arizona State University, Tempe, Arizona, 198 pp.
- Christensen, P.R., and S.T. Harrison, 1993, "Thermal infrared emission spectroscopy of natural surfaces: Application to desert varnish coatings on rocks," *J. Geophys. Res.*, vol. 98, pp. 19,819-19,834.
- Edgett, K.S., 1994, "The volcanoclastic Shifting Sand Dunes of Christmas Lake Valley, Oregon," in *The Sand Component of the Modern Martian Aeolian Sedimentary System*, Ph.D. Dissertation, Arizona State University, Tempe, AZ, pp. 145-201.
- Edgett, K.S., M.S. Ramsey, and P.R. Christensen, 1995, "Aeolian erosion, transport, and deposition of volcanoclastic sands among the Shifting Sand Dunes, Christmas Lake Valley, Oregon: TIMS image analysis," submitted for this volume.
- Hook, S.J., K.E. Karlstrom, C.F. Miller, and K.J.W. McCaffrey, 1994, "Mapping the Piute Mountains, California, with thermal infrared multispectral scanner (TIMS) images," *J. Geophys. Res.*, vol. 99, pp. 15,605-15,622.
- Ondrusek, J., P.R. Christensen, and J.H. Fink, 1993, "Mapping the distribution of vesicular textures on silicic lavas using the thermal infrared multispectral scanner," *J. Geophys. Res.*, vol. 98, pp. 15,903-15,908.
- Realmuto, V.J., 1990, "Separating the effects of temperature and emissivity: Emissivity spectrum normalization," in *Proceedings of the Second TIMS Workshop*, JPL Publication 90-55, pp. 31-35.
- Wang, Y., and B.R. Kowalski, 1992, "Calibration transfer and measurement stability of near-infrared spectrometers," *Applied Spectroscopy*, vol. 46, pp. 764-771.

AEOLIAN EROSION, TRANSPORT, AND DEPOSITION OF VOLCANICLASTIC SANDS AMONG THE SHIFTING SAND DUNES, CHRISTMAS LAKE VALLEY, OREGON: TIMS IMAGE ANALYSIS

Kenneth S. Edgett, Michael S. Ramsey, and Philip R. Christensen

Department of Geology, Arizona State University
Box 871404, Tempe, Arizona, 85287-1404, U.S.A.

1. INTRODUCTION

Remote sensing is a tool that, in the context of aeolian studies, offers a synoptic view of a dune field, sand sea, or entire desert region. Blount *et al.* (1990) presented one of the first studies demonstrating the power of multispectral images for interpreting the dynamic history of an aeolian sand sea. Blount's work on the Gran Desierto of Mexico used a Landsat TM scene and a linear spectral mixing model to show where different sand populations occur and along what paths these sands may have traveled before becoming incorporated into dunes. Interpretation of sand transport paths and sources in the Gran Desierto led to an improved understanding of the origin and Holocene history of the dunes (Blount and Lancaster, 1990).

With the anticipated advent of the EOS-A platform and ASTER thermal infrared capability in 1998 (Kahle *et al.*, 1991), it will become possible to look at continental sand seas and map sand transport paths using 8-12 μm bands that are well-suited to tracking silicate sediments. A logical extension of Blount's work is to attempt a similar study using thermal infrared images (Edgett *et al.*, 1994). One such study has already begun by looking at feldspar, quartz, magnetite, and clay distributions in the Kelso Dunes of southern California (Ramsey *et al.*, 1993, 1994). This paper describes the geology and application of TIMS image analysis of a less-well known Holocene dune field in south central Oregon using TIMS data obtained in 1991.

2. THE SHIFTING SAND DUNES, OREGON

The Shifting Sand Dunes are located in Christmas Lake Valley, at the eastern end of what was once the Pleistocene Fort Rock Lake. The basin is surrounded by Pliocene to Holocene basalt flows and mafic hyaloclastic tuffs. The ancient lake bed consists mainly of fluvio-lacustrine and volcanic airfall deposits. The bulk of the lake sediments are sand and silt-sized volcanic glass and crystals deposited by airfall; other sediments include diatomaceous earth, fine volcanic ash, basalt, and andesitic epiclasts (Dole, 1942). Much of the airfall sediment is considered to have come from eruptions of Mt. Mazama (now Crater Lake; Dole, 1942; Allison, 1979). During the Holocene, the lake bed surface has been reworked and shaped by wind, fluctuations in the levels of smaller lakes and ponds, and the deposition of large quantities of sandy ash that resulted from the terminal explosions of Mt. Mazama 6,800 years ago (Allison, 1979).

The dune area is about 30 km long and 10 km wide and contains a wide variety of bedforms. The dune field consists of two northeast-trending, megaparabolic dunes, one of which is very active today, the other is covered by trees and sagebrush comprising the Lost Forest Research Natural Area. Active dunes superposed on the megaparabolic structure include barchan and transverse forms that have linear ridges on them indicating a weak bimodal wind regime. Linear dunes, dome dunes, and parabolic dunes are also present. The main deflation areas occur at the western end of the dune field. The main active dune area has a deflation zone bounded by dune ridges and

contains Fossil Lake, an important Cenozoic fossil site. The dune field preserves a minimum of three major Holocene dune-building events (Edgett, 1994).

The main constituents of the Shifting Sand Dunes are volcanic glass and devitrified glass fragments, plagioclase crystals, basalt lithic fragments, aggregates of silt and clay-sized volcanic ash, pyroxenes, opaque minerals (mostly magnetite), and trace occurrences of fossil fragments and other minerals (Dole, 1942; Edgett, 1994). Most samples collected from the dunes in 1992 - 1994 contain nearly 50% plagioclase and 10 to 30% volcanic glass grains. The plagioclase is mostly andesine (Dole, 1942). The glass is mainly pumice shards, some of which have enclosed mineral crystals. Free crystals are mostly plagioclases and pyroxenes, and most of these have adhering glass and/or inclusions of glass, magnetite, or other minerals. The crystalline and glassy grains are generally angular to subangular, reflecting their original deposition as volcanic tephra. The volcanic ash aggregates are rounded to subrounded and are largely derived from erosion of a semilithified layer exposed in the deflation areas of the dune field. The volcanic lithic fragments are typically subrounded, probably indicating prior transportation by water. The Shifting Sand Dunes contain a mixture of sand deflated from the ancient lake bed plus sand-sized tephra deposited by the terminal eruptions of Mt. Mazama (Dole, 1942; Edgett, 1994).

3. TIMS IMAGE OF THE SHIFTING SAND DUNES

3.1 Data and Image Processing

The TIMS image of the Shifting Sand Dunes used in this study was acquired on September 21, 1991, by the NASA Ames Research Center C-130 Earth Resources Aircraft program. The C-130 had a mean altitude of 3657 m, resulting in an image with 9.1 m/pixel resolution at nadir. The raw image was converted to calibrated radiance, from which normalized emittance was computed for each of the six bands following the method of Realmuto (1990). Atmospheric attenuation effects along the margins of the image were reduced by subtracting a map of low frequency variation derived from a single-line low pass filter of 211 samples. Atmospheric effects were further removed by calibration transfer using laboratory spectra of material collected among the dunes (see Edgett and Anderson, 1995). The resulting 6-band image provides quantitative estimates of surface emissivity. The dune spectra in the image are consistent with spectra of samples from the same location as measured in the laboratory. The 6-band emissivity image was used in the two analyses which follow.

3.2 Surface 9.2 Micrometer Emissivity Image

Emissivity variations alone appear to be useful for distinguishing active and inactive dunes, interdunes, and deflation surfaces. TIMS band 3, in this case centered at 9.2 μm , provides the widest range in emissivities for the dune field (Figure 1). The entire range is only from 0.89 to 1.00, mostly concentrated between 0.90 and 0.95. Most of the emissivity variation results from the effects of surface composition, particle size, and vegetation. Vegetation has a high emissivity and relatively flat spectrum; most of the vegetation in the 9.2 μm image appears white (high emissivity). The lowest emissivities (0.89 to 0.91) correspond to the locations of active dune sand. Interdune areas have intermediate emissivities (0.90 to 0.95) which overlap on the low end with active sand and on the high end with vegetation. Interdune emissivities are a direct result of the material comprising the interdune surface, which in some places is sand and granules while in others is fine-grained ash and dry mud deposits. At the western end of the dune field in the vicinity of Fossil Lake, the large deflation area has low emissivities comparable to but generally a bit lower than the dunes (0.90 to 0.91). This deflation surface has a lag of granules and pebbles underlain by silt and sand. Further downwind (east), interdune emissivities rise; in some cases this is because the interdune is a dry pond with grasses and salts, in other areas, the interdune is a silty, semilithified lake bed layer from which ash aggregate grains are eroded and added to the dunes. Inactive

dunes are distinguished from active dunes because they have higher emissivities; although some have patches of active sand. Vegetation on inactive dunes has a higher emissivity, and vegetation traps dust, which also raises the emissivity.

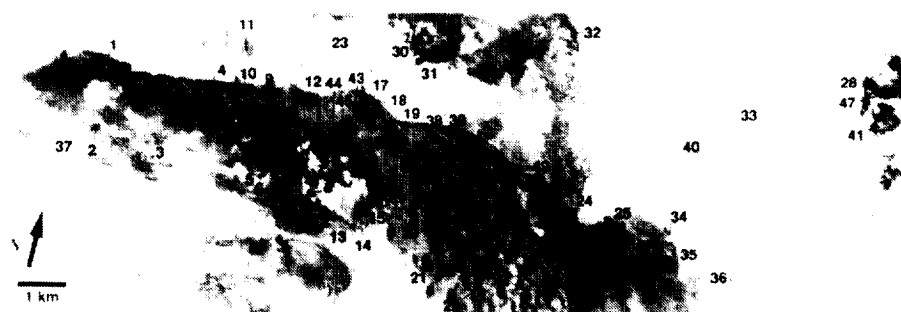


Figure 1. Emissivity image (9.2 μm) of main active portion of the Shifting Sand Dunes. Numbers indicate sample sites. Emissivities range from 1.0 (white) to 0.89 (dark gray).

3.3 Linear Unmixing Using Image Endmembers

Quantitative estimates of thermal infrared spectral emissivity are ideally suited for unmixing analysis. For grains larger than the wavelength (*i.e.*, dune sand), a linear unmixing approach can provide geologically useful results (Ramsey and Christensen, 1992a; Ramsey *et al.*, 1993, 1994). Such models are still in development and testing (Ramsey and Christensen, 1992b). Three types of endmembers can be selected: (1) spectra from pixels of different materials seen in the image, (2) laboratory spectra of materials collected from the field area in the TIMS scene, and (3) laboratory spectra of generic minerals in a spectral library. The present study follows the first approach, subsequent work will explore the latter two.

Five image endmembers were selected from the TIMS scene obtained in September 1991. Because there are no pure endmember materials in the scene, each selected here is a mixture of sub-endmembers. The first endmember is "regular sand," characterized by Dune 24 (Figure 1) with sub-endmembers: 48% plagioclase, 17% glass fragments, 9% ash aggregates, 12% volcanic lithic fragments, 9% pyroxene, and 5% opaques and others (from thin section analysis). "Regular sand" is the baseline against which other dune sands are compared. The second endmember consists of "mudchips," coarse aggregates of the silty volcanic ash derived from a capping layer among the lake sediments. The third endmember, "dark lithics," generally has abundant (> 25%) basalt grains and volcanic glass (> 30%). The fourth endmember consists of sagebrush and grass, which is distinct relative to the fifth endmember, "thick vegetation," which includes alfalfa crops and the pine trees of the Lost Forest.

The key result of this analysis is a map showing abundance of "regular sand" in the dune field relative to "mudchips" and "dark lithics." In the main active dune area, dark lithics are lags of granule-sized grains concentrated by wind, indicating areas of erosion near the base of dune ridges. The "mudchip" endmember represents surfaces with greater than 10% concentration of volcanic ash aggregate grains. Mudchips are most common in interdune areas at the middle of the main active dune area. Mudchips are eroded from the interdunes by the work of wind and off-road-vehicle usage and deposited locally on the dunes. Using the TIMS to identify and map mudchip (volcanic ash aggregate) contributions to the dunes represents a new approach to identifying local sources of sand in terrestrial dune fields. The unmixing analysis also has shown that the active dunes at the remote eastern end of Figure 1, within the Lost Forest, contain more

basalt fragments than the main active dune area. The basalt in this case appears to be a local contribution from the erosion of mafic tuffs in the vicinity.

The distribution of mudchips and dark lithics in the mixing image follows a lineated pattern reflective of the ridges superposed on most of the dunes in the area. The dune ridges result from a season-dependent, weakly bimodal wind regime; the mixing pattern reflects the variation of erosion and deposition on dune surfaces among the dunes. Future work will attempt to use grains collected from the dunes for unmixing analysis. Because of the abundance of glass and microcrystalline material in these sands, the Shifting Sand Dunes represent an intriguing and somewhat more complex problem for mixing studies than do the Kelso Dunes examined by Ramsey *et al.* (1993, 1994).

4. REFERENCES

- Allison, I.S., 1979, *Pluvial Fort Rock Lake, Lake County, Oregon, Special Paper*, no. 7, Oregon State Department of Geology and Mineral Resources, 72 pp.
- Blount, G., and N. Lancaster, 1990, "Development of the Gran Desierto Sand Sea," *Geology*, vol. 18, pp. 724-728.
- Blount, G., M.O. Smith, J.B. Adams, R. Greeley, and P.R. Christensen, 1990, "Regional aeolian dynamics and sand mixing in the Gran Desierto: Evidence from Landsat thematic mapper images," *J. Geophys. Res.*, vol. 95, pp. 15,463-15,482.
- Dole, H.M., 1942, *Petrography of Quaternary lake sediments of northern Lake County, Oregon*, M.S. Thesis, Oregon State College, Corvallis, Oregon, 98 pp.
- Edgett, K.S., 1994, "The volcanoclastic Shifting Sand Dunes of Christmas Lake Valley, Oregon," in *The Sand Component of the Modern Martian Aeolian Sedimentary System*, Ph.D. Dissertation, Arizona State University, Tempe, AZ, pp. 145-201.
- Edgett, K.S., and D.L. Anderson, 1995, "For geologic investigations with airborne thermal infrared multispectral images: Transfer of calibration from laboratory spectrometer to TIMS as alternative for removing atmospheric effects," submitted for this volume.
- Edgett, K.S., P.R. Christensen, and M.S. Ramsey, 1994, "Monitoring aeolian dune dynamics using multispectral thermal infrared observations: Preparing for the Earth Observing System's Advanced Spaceborne Thermal Emission and Reflectance Radiometer," *Abstracts of a Workshop on the Response of Eolian Processes to Global Change, Desert Research Institute Quaternary Sciences Center Occasional Paper*, no. 2, pp. 29-31.
- Kahle, A.B., F.D. Palluconi, S.J. Hook, V.J. Realmuto, and G. Bothwell, 1991, "The Advanced Spaceborne Thermal Emission and Reflectance Radiometer (ASTER)," *Internat. J. Imaging Syst. Tech.*, vol. 3, pp. 144-156.
- Ramsey, M.S., and P.R. Christensen, 1992a, "Ejecta patterns of Meteor Crater, Arizona, derived from the linear un-mixing of TIMS data and laboratory thermal emission spectra," in *Summaries of the Third Annual JPL Airborne Geoscience Workshop, TIMS Workshop*, vol. 2, JPL Publication 92-14, pp. 34-36.
- Ramsey, M.S., and P.R. Christensen, 1992b, "The linear 'unmixing' of laboratory thermal infrared spectra: Implications for the Thermal Emission Spectrometer (TES) experiment, Mars Observer," *Lunar Planet. Sci. XXIII*, pp. 1127-1128.
- Ramsey, M.S., D.A. Howard, P.R. Christensen, and N. Lancaster, 1993, "Mineralogic variability of the Kelso Dunes, Mojave Desert, California, derived from Thermal Infrared Multispectral Scanner (TIMS) data," in *Summaries of the Fourth Annual JPL Airborne Geoscience Workshop, TIMS Workshop*, vol. 2, JPL Publication 93-26, pp. 9-12.
- Ramsey, M.S., D.A. Howard, P.R. Christensen, and N. Lancaster, 1994, "Sand sources and mineralogic variability within the Kelso Dune field, Mojave Desert, California: Analysis of thermal remote sensing data," *Abstracts with Programs, Geological Society of America Annual Meeting*, vol. 26, pp. 89.
- Realmuto, V.J., 1990, "Separating the effects of temperature and emissivity: Emissivity spectrum normalization," in *Proceedings of the Second TIMS Workshop, JPL Publication 90-55*, pp. 31-35.

The JPL Field Emission Spectrometer

Simon J. Hook and Anne B. Kahle
 Jet Propulsion Laboratory
 California Institute of Technology
 Pasadena, CA 91109

The Jet Propulsion Laboratory (JPL) Field Emission Spectrometer (FES) was built by Designs and Prototypes based on a set of functional requirements supplied by JPL. The instrument has a spectral resolution of 6 wavenumbers (wn) and can acquire spectra from either the Mid Infrared (3-5 μm) or the Thermal Infrared (8-12 μm) depending on whether the InSb or HgCdTe detector is installed respectively. The instrument consists of an optical head, system unit and battery. The optical head, which is tripod mounted, includes the interferometer and detector dewar assembly. Wavelength calibration of the interferometer is achieved using a Helium-Neon laser diode. The dewar needs replenishing with liquid Nitrogen approximately every four hours. The system unit includes the controls for operation and the computer used for acquiring, viewing and processing spectra. Radiometric calibration is achieved with an external temperature-controlled blackbody that mounts on the fore-optics of the instrument. The blackbody can be set at 5 °C increments between 10 and 55 °C. The instrument is compact and weighs about 33 kg. Both the wavelength calibration and radiometric calibration of the instrument have been evaluated. The wavelength calibration was checked by comparison of the position of water features in a spectrum of the sky with their position in the output from a high resolution atmospheric model. The results indicate that the features in the sky spectrum are within 6-8 wn of their position in the model spectrum. The radiometric calibration was checked by first calibrating the instrument using the external blackbody supplied with the instrument and then measuring the radiance from another external blackbody at a series of temperatures. The temperatures of these radiance spectra were then recovered by inverting Planck's law and the recovered temperatures compared to the measured blackbody temperature. These results indicate that radiometric calibration is good to 0.5 °C over the range of temperatures 10 to 55 °C. The results also indicate that the instrument drifts slowly over time and should be recalibrated every 20 to 30 minutes in the field to ensure good radiometric fidelity.

The instrument has now been extensively tested in the field in the United States and Australia. These in situ field measurements are being used to validate emissivity spectra recovered from the Thermal Infrared Multispectral Scanner (TIMS) and also the Australian CO₂ Laser. The availability of in situ measurements is proving crucial to validation of the spectra derived from the airborne instruments since many natural surfaces cannot be easily transported back to the laboratory.

ACKNOWLEDGMENTS

The research described in this paper was carried out in full at the Jet Propulsion Laboratory, California Institute of Technology, under a contract with the National Aeronautics and Space Administration.

Reference herein to any specific commercial product, process, or service by trade names, trademark, manufacturer or otherwise does not imply endorsement by the United States or the Jet Propulsion Laboratory, California Institute of Technology.



"A CONFLICT OF WATER AND FIRE": REMOTE SENSING IMAGERY OF THE UINKARET VOLCANIC FIELD, GRAND CANYON, ARIZONA

Michael S. Ramsey
Department of Geology
Arizona State University
Tempe, Arizona 85287-1404

1. INTRODUCTION

"What a conflict of water and fire there must have been here! Just imagine a river of molten rock running down a river of molten snow."

*J.W. Powell
August 25, 1869*

The geology of the western Grand Canyon represents perhaps the most spectacular three dimensional displays of volcanological processes in the world. The dramatic sight of frozen basaltic lava falls cascading over the Canyon's inner gorge was first documented during John W. Powell's initial expedition into the region in 1869 (Powell, 1873). Over the past two million years, lavas have erupted from both fissures and central vents, forming the Uinkaret volcanic field. At the southern reach of this tectonically controlled lava field lies the Colorado River and the Grand Canyon. Lavas that erupted close to the edge of the rim flowed down it forming cascades over 900 meters high (Hamblin, 1994). In addition to this activity, multiple vents erupted within the Canyon itself. The products of this activity effectively dammed the river 13 times; the remnants of which are still visible along the Canyon walls today. The largest of the dams formed a 700 meter deep lake which extended up river into present day Utah. Geological investigations of the Uinkaret field, the lava cascades and the remains of the basaltic dams have been relatively few (Koons, 1945; Maxon, 1950; Hamblin, 1994) despite the remarkable nature of the geology. Previous investigations have been hindered by the remoteness of the site and near impossibility of accessing most of the flows.

In addition to the geological interest of this region, the Colorado River, its beaches and riparian habitats are under more intense study in an attempt to document the impact of human damming of the river. As a result of the construction of the Glen Canyon Dam, the average water temperature has dropped over 20 degrees Fahrenheit during the past 30 years. Sediment load, vital for beach replenishment and stabilization has been cut off. The result is a Colorado River that now runs clear and cold where once it ran cloudy and warm. Finally, human use of the Grand Canyon and Colorado River by way of recreational activities like rafting is at an all time high, with tens of thousands of people per year enjoying the Colorado by boat. The need for large scale, relatively inexpensive monitoring of the river and its surrounding environments is evident.

2. GEOLOGICAL SETTING

The sedimentary geology of the western Grand Canyon consists of gently northeast dipping sandstones, shales and carbonates. However, due to facies changes within the units, the geomorphology varies from that seen by visitors at the National Park Headquarters. There, the cliff and slope expression of the rocks is replaced in the

west by a series of mesas, ridges and horizontal platforms. The largest of these occurs on the Esplanade Sandstone within the Supai Formation. The Esplanade is formed by slope retreat of the overlying units and resistance to erosion by the underlying limestones. It is onto this platform that the lavas of the Uinkaret Plateau were emplaced.

The Uinkaret lava field lies 120 km south of St. George, Utah and is tectonically defined by two major normal faults - the Hurricane to the west and the Toroweap to the east. As the surficial expression of these faults converge to 15 km at the Canyon, the concentration of the volcanic centers increase (Hamblin, 1974). Very few of the actual vents lie directly on the faults, however. The regional stresses associated with fault formation opened north-south trending fissures which accommodated magma rise. The basaltic lava flows were extremely numerous during the height of activity 1.8 m.y. Volumes of most eruptions were rather small and resulted in thin, short flows. The total volume of the lava field was enough to fill the Toroweap and Whitmore valleys to the level of the Esplanade (> 650 m). Eruptions close to the edge of the inner gorge flowed over the rim producing the many lava cascades visible today. Vents that formed within the gorge itself gave rise to the multiple damming events of the river. These dams occurred over a period of 1.4 m.y. and in each case were breached and eroded by the Colorado River in less than 20,000 years (Hamblin, 1994). Prospect, the largest and oldest dam, when overtopped, had a waterfall over 600 meters high with a volume 20 times that of Niagra Falls. The fault system remains active today, but the last eruption of the Uinkaret field occurred over 200,000 years ago.

3. DATA COLLECTION AND ANALYSIS

The purpose of this investigation was to collect visible, near and thermal infrared data at different periods of the day and year. It is expected that these data will provide the ability to retrieve water temperatures; monitor sediment loads; map and examine any changes in the near shore vegetation communities and understand some of the intricacies of the geology. This paper will serve, to some degree, as a progress report on the Grand Canyon study, since only a fraction of the data has been received and processed thus far.

Data from the Thermal Infrared Multispectral Scanner (TIMS) and the Landsat Thematic Mapper Simulator (NS001) were acquired simultaneously on April 4, 1994. The flight line ran along the Colorado in a roughly southeast to northwest direction and covered over 20 river miles. The altitude of 17,000 feet (5.18 km) above ground level produced an image resolution of 13 m/pixel at nadir. The higher altitude was chosen to provide coverage of both the river and shore environments as well as capturing a large portion of the volcanic field and exposed sedimentary units of the Grand Canyon. A second data acquisition occurred on August 27, 1994. The late summer data were acquired at night with the intent of examining seasonal variations as well as to produce a thermal inertia map of the region. At present, only a preliminary examination the spring data has been performed. This data set will provide baseline for monitoring the area and will be used to assess the viability of future data acquisitions at higher spatial resolutions.

Initial analysis of the TIMS data indicates a remarkably noise-free data set with minimal atmospheric attenuation. Standard decorrelation processing (Gillespie, 1986) clearly distinguishes the petrologic variations of the diverse lithology in the scene. Further, significant color variations within the lava fields themselves may indicate subtle differences in lava composition, age and/or surface textures. These variations, if indicative of petrologic or age differences, may improve the understanding and constrain the stratigraphy and timing of the damming events (McKee, et al., 1968). The primary

tectonic features, the Hurricane and Toroweap faults, control of the location of the Uinkaret field and are easily discernible in both the TIMS and NS001 images. At river level, the 400 meters of displacement along the Hurricane Fault places the Pennsylvanian Supai Formation in contact with the Cambrian Muav Limestone. Detailed examination of beach and talus along the both sides of the river indicate that little net transport of material occurs from one side of the Colorado to the other. Sand and gravel derived from the Cenozoic volcanics are confined to the northern side, while the south is comprised primarily of carbonate and sandstone detritus.



Figure 1. Western Grand Canyon TIMS imagery acquired on April 4, 1994. The image size is approximately 24 km long by 9.5 km wide with N oriented to the lower right. Both images are the product of the separation of radiant flux into emissivity and temperature. **A.** Band 3 emissivity image (dark grey to black indicate rock outcrops with strong absorptions at $9.2 \mu\text{m}$ such as the Coconino Sandstone). **B.** Kinetic temperature image. Derived temperatures range from 57°F (14°C) on portions of the river to 167°F (75°C) on a sun-facing slope of one of the basalt flows.

The data were also separated into normalized emissivity (Realmuto, 1990; Kannari, et al., 1991) and kinetic temperature images (Fig. 1). Distinct spectral absorption features of the major rock forming units are indicative of the petrologic variability of the scene, the near 100% exposure of the rocks, and the high signal to noise of the data. These spectra will be used as input endmembers into a linear, spectral retrieval model in order to determine subpixel abundances (Ramsey, et. al., 1994) and

track sediment addition and transport by the Colorado River. The moderate spatial resolution of the data may prove to be a hindrance when mapping temperature fluctuations along the length of the river. Detectable drops in temperature of several degrees occur over the major rapids such as Lava Falls. However, because the river is only several pixels wide in the image, variations along its length may be due to pixel overlap with the shoreline.

4. ACKNOWLEDGEMENTS

This work was supported under P.R. Christensen by NASA grant NAS5-31371. I would like to thank the entire crew of the NASA C130 aircraft program for their extra effort and dedication in acquiring both data sets, as well as Rich Peace who made my last trip down the Colorado a reality, the result of which sparked my interest in the region.

5. REFERENCES

- Gillespie, A.R., Kahle, A.B., and Walker, R., 1986, "Color enhancement of highly correlated images: I. Decorrelation and HSI contrast stretches," *Remote Sensing Environ.*, v. 20, pp. 209-235.
- Hamblin, W.K., 1994, *Late Cenozoic Lava Dams in the Western Grand Canyon*, Geological Society of America Memoir 183, The Geological Society of America, Boulder, Colorado, pp. 1-110.
- Hamblin, W.K., 1974, *Late Cenozoic Volcanism in the Western Grand Canyon*, in *Geology of the Grand Canyon: Breed, W.J. and Roat, E.C., eds.*, Museum of Northern Arizona/Grand Canyon National History Association, pp. 142-170.
- Kannari, Y., Mills, F.P., and Wantanabe, H., 1991, "Results by a Normalization Method Applied to TIMS Data for Cuprite, Nevada", in *Proc. of the Third TIMS Workshop*: Abbott, E.A., ed., JPL Pub. 91-29, JPL, Pasadena, Calif., pp. 45-53.
- Koons, E.D., 1945, "Geology of the Uinkaret Plateau, Northern Arizona," *Geol. Soc. Am. Bull.*, vol. 56, pp. 135-161.
- Maxon, J.H., 1950, "Lava Flows in the Grand Canyon of the Colorado River, Arizona," *Geol. Soc. Am. Bull.*, vol. 61, pp. 9-15.
- McKee, E.D., 1942, "The Lower Canyon Lavas and Related Features at Toroweap in the Grand Canyon," *J. Geomorph.*, vol. 5, pp. 245-273.
- Powell, J.W., 1873, "Exploration of the Colorado River of the West and its Tributaries Explored in 1869-1872," Washington, D.C., Smithsonian Institution, pp. 94-196.
- Ramsey, M.S., Howard, D.A., Christensen, P.R., and Lancaster, N., 1994, "Thermal Remote Detection of Sand Sources for, and Mineralogic Variability Within, the Kelso Dune Field, Mojave Desert, California," in *Geol. Soc. Am. Abs. with Programs*, vol. 26, no. 7, 1994 Annual Meeting, pp. A 89.
- Realmuto, V.J., 1990, "Separating the Effects of Temperature and Emissivity: Emissivity Spectrum Normalization", in *Proc. of the Second TIMS Workshop*: Abbott, E.A., ed., JPL Pub. 90-55, JPL, Pasadena, Calif., pp. 26-30.

CAPTION FOR TIMS WORKSHOP SLIDE 1

Thermal Infrared Multispectral Scanner (TIMS) decorrelation stretch image of bands 431 in RGB respectively. The scene covers approximately 9.5 km x 15 km, from river mile 182 to 192, with north to the lower right of the slide. The Esplanade Sandstone of the Supai Fmt. forms the prominent horizontal platform displayed in yellow-orange. The deep green of the inner gorge marks the location of early Paleozoic limestones of the lower Grand Canyon sequence. Several cinder cones in the lower right of the slide lie at the southwest margin of the Uinkaret volcanic field. Basaltic flows (shown in blue) from these and other vents filled the 650 meter deep Whitmore wash (right center of slide) and produced the lava cascades within the inner gorge. Hurricane Fault, the western tectonic boundary of the Uinkaret field, can easily be located striking southward from Whitmore wash towards the upper left corner of the slide.

THE 1994 LABORATORY CALIBRATION OF TIMS

Vincent J. Realmuto, Pavel Hajek, Mahadeva P. Sinha, and Thomas G. Chrien

Jet Propulsion Laboratory, California Institute of Technology
Pasadena, CA 91109

1. INTRODUCTION

This summary describes the spatial, spectral, and radiometric calibration of Thermal Infrared Multispectral Scanner (TIMS) performed at the Jet Propulsion Laboratory (JPL) Thermal Infrared Calibration Facility (TIRCAL) between May and August, 1994. The 1994 calibration of TIMS was the first to make use of the new EXABYTE (8mm helical-scan tape) recording system. With the new recorder, the TIMS data tapes may be read directly on any computer system that has an EXABYTE tape drive. We analyzed the calibration data sets using image processing procedures written in Interactive Data Language (IDL, Research Systems, Inc., Boulder, CO 80303).

2. SPATIAL CALIBRATION

The purpose of the spatial, or geometric, calibration was to verify the instantaneous field of view (IFOV) of TIMS in the scan line, or horizontal, and flight line, or vertical, directions. The equipment required for the spatial calibration tests included a large flat mirror with a 45° mount, a collimator (1 m focal length), a translation stage (with controller), thin (0.3 mm diameter) nickel-chromium (NiCr) wire, an oscilloscope, and various power supplies. The accuracy and precision of the translation rate of the translation stage was determined with a micrometer and stop watch.

TIMS was mounted on a support frame approximately 0.3 m above the surface of an optical bench. The mirror was positioned beneath TIMS to reflect the output of the collimator into the instrument. The NiCr wire was mounted on the translation stage and heated to incandescence. The hot wire was positioned next to the input port of the collimator such that the image of the wire was in the focal plane of the collimator. The optimum alignment of the folding mirror was found by moving the mirror and checking the TIMS response with the oscilloscope.

The hot wire was translated in both the horizontal and vertical directions, relative to the collimator. The movement of the hot wire across the TIMS field stop mapped the field stop into the image data. Profiles of these data taken perpendicular to the TIMS scan direction resembled Gaussian functions. The width of these functions at half the maximum amplitude (full width-half maximum, or FWHM) was a measure of the IFOV of TIMS. The following table summarizes the results of the spatial calibration.

TIMS Channel	Horizontal IFOV (mrad)	Vertical IFOV (mrad)
1	2.65 ± 0.096	2.58 ± 0.093
2	2.66 ± 0.094	2.64 ± 0.093
3	2.62 ± 0.095	2.50 ± 0.093
4	2.61 ± 0.090	2.71 ± 0.095
5	2.54 ± 0.096	2.69 ± 0.095
6	2.49 ± 0.105	2.56 ± 0.094

3. SPECTRAL CALIBRATION

The equipment required for the spectral calibration of TIMS was similar to that required for the spatial calibration, with the substitution of a monochromator and infrared glower (source) for the hot wire and translation stage. The spectral and radiometric characteristics of the monochromator and glower were determined prior to the spectral calibration of TIMS. The accuracy and precision of the monochromator scan rate was also determined.

The monochromator was positioned at the input port of the collimator such that the monochromator slit was in the focal plane of the collimator. The monochromator was scanned between 7 and 13 μm . Profiles of the TIMS data taken perpendicular to the scan direction produced "raw" spectral response functions for each TIMS channel. Knowledge of the scan rates of the monochromator (μm per second) and TIMS (scans per second) allowed us to determine the spectral output of the monochromator at each TIMS scan line. The raw response functions were filtered to remove noise and corrected for the spectral and radiometric responses of the monochromator and glower. The results of the spectral calibration are summarized in the following table, and a plot of the response functions is found in Figure 1. The tabulated response functions are available upon request.

TIMS Channel	FWHM (μm)	Peak Position (μm)
1	0.374 ± 0.011	8.402 ± 0.050
2	0.358 ± 0.013	8.766 ± 0.052
3	0.379 ± 0.016	9.212 ± 0.055
4	0.690 ± 0.021	10.012 ± 0.060
5	0.888 ± 0.028	10.630 ± 0.063
6	0.659 ± 0.035	11.512 ± 0.068

4. RADIOMETRIC CALIBRATION

For the radiometric phase of the calibration, an extended-area blackbody was positioned below the TIMS support frame. The large surface area of the blackbody completely filled the TIMS aperture. The purpose of the radiometric calibration was to determine if the TIMS estimates of the blackbody temperatures agreed with the temperatures set on the blackbody controller.

4.1. Radiometric Precision

The uniform temperature distribution across the surface of the extended-area blackbody allowed us to evaluate the radiometric precision of TIMS, which is usually reported as the noise equivalent delta temperature ($\text{NE}\Delta\text{T}$). The $\text{NE}\Delta\text{T}$ is the smallest change in temperature that TIMS can discriminate in the presence of noise. Analogously, the deviation in TIMS temperature estimates over a surface with a uniform temperature distribution is a measure of the $\text{NE}\Delta\text{T}$.

Figure 2 is a plot of the standard deviations of temperature estimates in each of the six TIMS channels against the temperature of the extended-area blackbody (Channel 1 = +, 2 = *, 3 = \diamond , 4 = Δ , 5 = \square , 6 = X). At the level of one standard deviation, the $\text{NE}\Delta\text{T}$ is better than 0.17 $^{\circ}\text{C}$ in all six TIMS channels.

4.2. Radiometric Accuracy

Figure 3 is a plot of the TIMS temperature estimates for the extended-area blackbody against the set-point temperatures of the blackbody. The experiments were performed at two different combinations of settings for the reference blackbodies internal to TIMS. The solid line (Fig. 3) represents the TIMS temperature estimates recovered with internal settings of 20 and 45 °C, while the broken line represents the TIMS temperature estimates recovered with internal settings of 25 and 50 °C. The latter settings prevented TIMS from saturating when observing high-temperature surfaces.

In general, the TIMS estimates were slightly higher than the set-point temperatures. This effect was slightly more pronounced when the internal blackbodies were set to 25 and 50 °C. However, the TIMS temperature estimates were within 0.8 °C of the set-point temperatures for all of our calibration experiments.

5. CONCLUSIONS

The results of our calibration experiments indicate that TIMS is capable of estimating surface temperatures with an absolute accuracy of 1.0 °C. The instrument can detect changes in surface temperature of at least 0.2 °C for a surface temperature ranging between 20 and 45 °C. These conservative accuracy levels are based on the worst-case results of the calibration experiments.

It is important to realize that these accuracy levels were achieved in the absence of a turbulent wind blast (aside from the air-flow generated by the TIMS scan mirror). In addition, we had a short atmospheric path (< 0.5 m) and near-complete knowledge of the emissivity of our target surface. The in-flight accuracy of TIMS, with turbulent winds in the instrument bay, long paths through the atmosphere, and incomplete knowledge of the emissivity of the ground, will certainly be lower than the laboratory accuracy.

ACKNOWLEDGMENT

The research described in this paper was performed at the Jet Propulsion Laboratory, California Institute of Technology, under a contract to the National Aeronautics and Space Administration.

Reference herein to any specific commercial product, process, or service by trade names, trademarks, manufacturer, or otherwise does not imply endorsement by the United States or the Jet Propulsion Laboratory, California Institute of Technology.

FIGURE 1: TIMS SPECTRAL RESPONSE

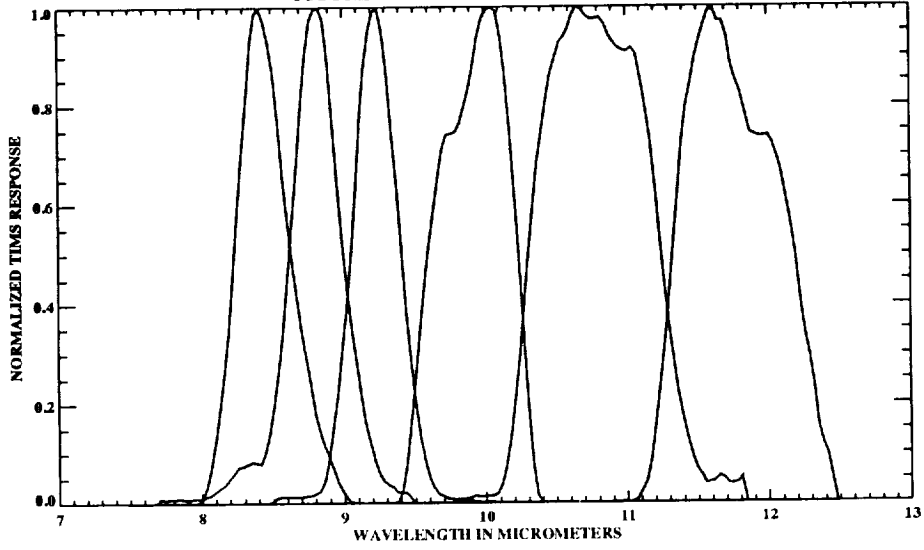


FIGURE 2: TIMS RADIOMETRIC PRECISION

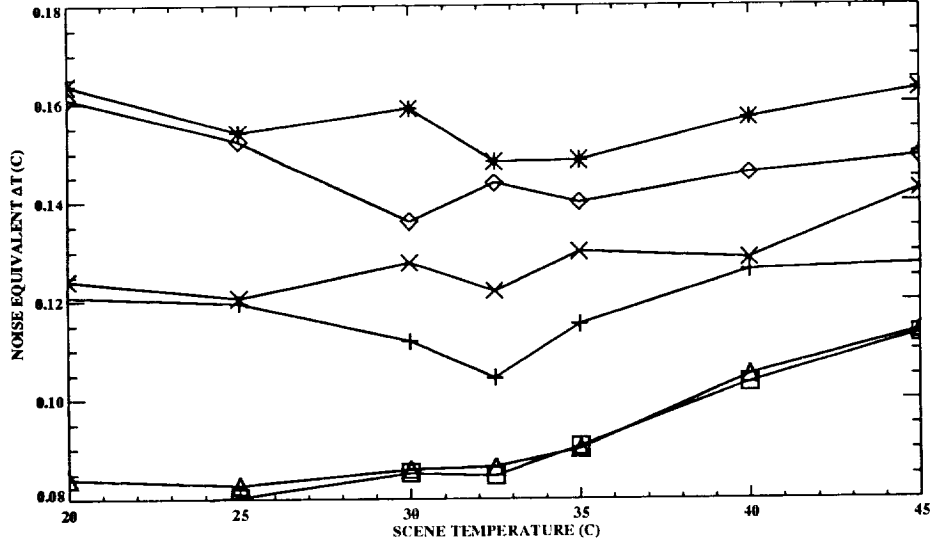
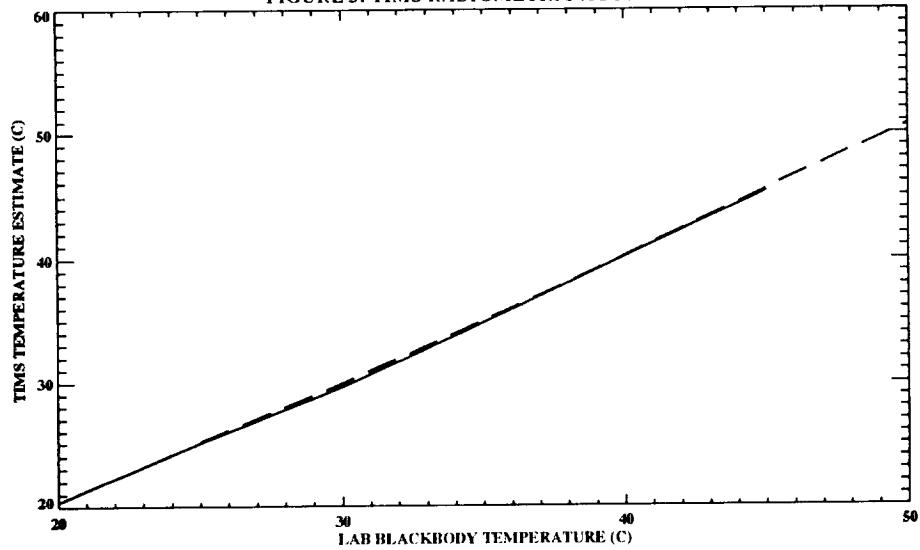


FIGURE 3: TIMS RADIOMETRIC ACCURACY



THE 1994 TIMS AIRBORNE CALIBRATION EXPERIMENT: CASTAIC LAKE, CALIFORNIA

Vincent J. Realmuto, Simon J. Hook, and Jeannette van den Bosch

Jet Propulsion Laboratory, California Institute of Technology
Pasadena, CA 91109

1. INTRODUCTION

This summary describes the 9 March 1994 Thermal Infrared Multispectral Scanner (TIMS) airborne calibration experiment conducted at Castaic Lake, California. This experiment was a collaborative effort between the TIMS and Advanced Spaceborne Thermal Emission and Reflection Radiometer (ASTER) science teams at the Jet Propulsion Laboratory (JPL). TIMS was flown on the NASA/Ames Research Center C-130 with the new retractable air fence installed in the TIMS instrument bay. The purpose of this experiment was to determine if the fence would reduce the air turbulence in the TIMS instrument bay, thereby reducing the errors in calibration caused by wind-blast cooling of the blackbody reference sources internal to TIMS. Previous experiments have indicated that the wind blast effect could cause TIMS to over-estimate surface temperatures by more than 10 °C.

We have examined the TIMS data from twelve lines flown over Castaic Lake. Four of the lines were flown at an altitude of ~2.5 km (MSL), four at an altitude of ~6.7 km, and four at ~8.3 km. At each altitude there were flights with northern and southern headings, with the aircraft level and at a positive pitch (nose-up attitude). The suite of twelve flights was designed to subject the TIMS/air fence system to different wind conditions and air temperatures.

The TIMS flights were supported by a ground-truth team, who measured lake surface temperatures from a boat, and an atmosphere characterization team, who launched an airsonde and measured solar irradiance with a Reagan Sun Photometer. The Reagan measurements were used to construct a time-series of estimates of the total abundance of water vapor in the atmospheric column. These estimates were used to constrain modifications of the airsonde water vapor profile measurements made when processing the TIMS data with a customized version of the MODTRAN radiative transfer code.

2. DESCRIPTION OF EXPERIMENT AND DATA REDUCTION

Castaic Lake is located approximately 56 km northwest of JPL. Magic Mountain Amusement Park, the site of the airsonde launch and the Reagan photometric measurements, is approximately 10 km south of Castaic Lake. A failure of the battery pack powering the airsonde receiver terminated the atmosphere profile measurements at an altitude of approximately 5 km. The pressure, temperature, and relative humidity values from the mid-latitude summer climatic model of MODTRAN were used to augment the airsonde profile at altitudes greater than 5 km. Despite the equipment problems, the airsonde measurements did cover the crucial region below 5 km which contains over 90% of the atmospheric water vapor.

We have long recognized that a single airsonde profile cannot describe the spatial variation in atmospheric water vapor within a single TIMS scene or the temporal variation between successive scenes. In addition, the absolute accuracy of the carbon hygrometers used to measure relative humidity is not known (the manufacturer's calibration is performed at a single relative humidity level of 33%). We attempted to verify our airsonde measurements by using a Reagan Sun Photometer to obtain a time-series of

estimates of water vapor column abundance. While the airsonde profile is probably an accurate estimate of the relative vertical distribution of water vapor in the atmosphere, the photometer measurements suggest that the airsonde over-estimated the total column abundance of water vapor.

To correctly process TIMS data, we must often modify the column abundance of water vapor in an airsonde (or radiosonde) profile prior to running the radiative transfer code. The constraint on this modification is to achieve an agreement between the temperature estimates in the six TIMS channels over an extended water target, which we assume to have a flat emissivity spectrum (emissivity equal to 1.0 in each TIMS channel) and uniform surface temperature distribution. If our assumptions are correct, then we can attribute disagreements between the channel temperature estimates to atmospheric effects and modify the profile accordingly. Our photometer measurements of water vapor column abundance were used to further constrain the modification of the airsonde profile to process the data from each of the TIMS flights.

Prior to processing the TIMS data, MODTRAN was run with the airsonde profile to determine the apparent total (surface to 9 km altitude) column abundance of water vapor. To process the data from each flight, MODTRAN was run with the airsonde profile to determine the apparent amount of water vapor between TIMS and the lake surface. This quantity was divided by the apparent total column abundance to determine the fraction of the total between TIMS and the lake surface. This fraction was used to scale the corresponding Reagan total column water vapor measurement. MODTRAN was then run a second time, with a scaling factor applied to the airsonde profile to bring the water vapor column abundance reported by MODTRAN into agreement with the scaled Reagan measurement. This processing strategy allowed us to accommodate temporal variations in the total water vapor content of the atmosphere, but we did not accommodate temporal or spatial variations in the vertical or horizontal distribution of water vapor. We used the mid-latitude summer ozone profile packaged with MODTRAN to process the TIMS data.

3. DISCUSSION OF RESULTS

The ground-truth team collected 49 measurements of lake surface temperatures, using two infrared radiant thermometers and a single boat. This sample of lake surface temperatures has a mean of 14.6 °C and a standard deviation of 0.3 °C.

3.1. Surface Temperatures Acquired from an Altitude of 2.5 km

Figure 1 is a plot of the one standard deviation spread in the ground-truth temperature measurements (broken lines) and TIMS temperature estimates from an altitude of 2.5 km (solid lines). The TIMS temperature estimates were derived from 145 X 145 pixel subareas of the four Castaic Lake scenes. The TIMS precision envelope encloses the mean estimates plus or minus the corresponding standard deviations from all four flight lines. The TIMS temperature estimates in all six channels agree with the ground truth, within the level of precision of the measurements. It is interesting to note that the TIMS temperature estimates acquired from 2.5 km have larger standard deviations than those acquired from the higher altitudes. This phenomena is in part due to variations in the surface temperature of Castaic Lake resulting from wave action and boat traffic.

3.2. Surface Temperatures Acquired from an Altitude of 6.7 km

Figure 2 compares the precision of the temperatures acquired from the four 6.7 km flights and the ground-truth temperature measurements. The TIMS temperature estimates were derived from subareas of 55 X 55, 65 X 65, and 85 X 85 pixel subareas. As in Figure 1, the envelopes enclose one standard deviation of the variation in measurements. The TIMS temperature estimates in all six channels agree with the ground-truth within the precision level of the measurements.

3.3. Surface Temperatures Acquired from an Altitude of 8.2 km

Figure 3 compares the precision of the temperatures acquired from the four 8.2 km flights and the ground-truth temperature measurements at the level of one standard deviation. The temperature estimates for all of the flights are the mean values of 45 X 45 pixel subareas. The TIMS temperature estimates in Channels 2, 3, 4, and 6 agree with the ground-truth within the precision level of the measurements. The disagreement in Channel 1 is most likely due to the combined effects of errors in estimates of water vapor abundance and wind-blast cooling of the TIMS blackbody references. The disagreement in Channel 5 is most likely due to the cooling effect.

4. CONCLUSIONS

The general progression in surface temperature estimates with flight altitude suggests that there is some remaining wind-blast cooling of the TIMS blackbody references when the air fence is deployed. Over-estimation of the water vapor abundance of the atmosphere can likewise cause the temperature estimates to increase with increasing altitude. The apparent increases in ground temperature between the lowest temperatures acquired from 2.5 km and the highest temperatures acquired from 8.3 km are less than 1.5 °C in Channels 2 through 6. For Channel 1, which is most strongly affected by water band absorption, this increase is 2.5 °C. Refinements in our assessment of the accuracy of TIMS will follow improvements in our calibration experiment procedure; we must make efforts to improve our ability to characterize both the atmosphere and our ground targets.

Based on the 9 March 1994 experiment, we conclude that the C-130 air fence has greatly reduced the TIMS calibration problem by reducing the wind turbulence in the TIMS instrument bay. Given supporting airsonde (or radiosonde) launches and solar photometry, together with favorable weather conditions, investigators should be able to recover ground temperature estimates with an absolute accuracy of 2.0 °C. This conservative accuracy range, based largely on the results for Channel 1, accommodates (1) remaining wind-blast cooling of the TIMS blackbody references, (2) inaccuracies in our characterization of the atmosphere, and (3) variations in the surface temperature of Castaic Lake due to boat traffic and wave action.

ACKNOWLEDGMENT

The research described in this paper was performed at the Jet Propulsion Laboratory, California Institute of Technology, under a contract with the National Aeronautics and Space Administration.

Reference herein to any specific commercial product, process, or service by trade names, trademark, manufacturer, or otherwise does not imply endorsement by the United States or the Jet Propulsion Laboratory, California Institute of Technology.

FIGURE 1: GROUND TEMPS FROM 2.5 KM ALTITUDE (MSL)

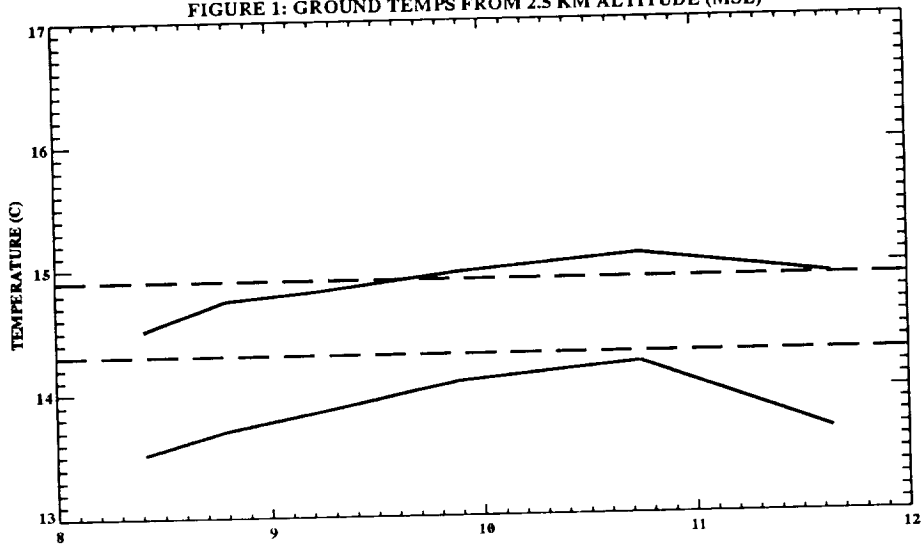


FIGURE 2: GROUND TEMPS FROM 6.7 KM ALTITUDE (MSL)

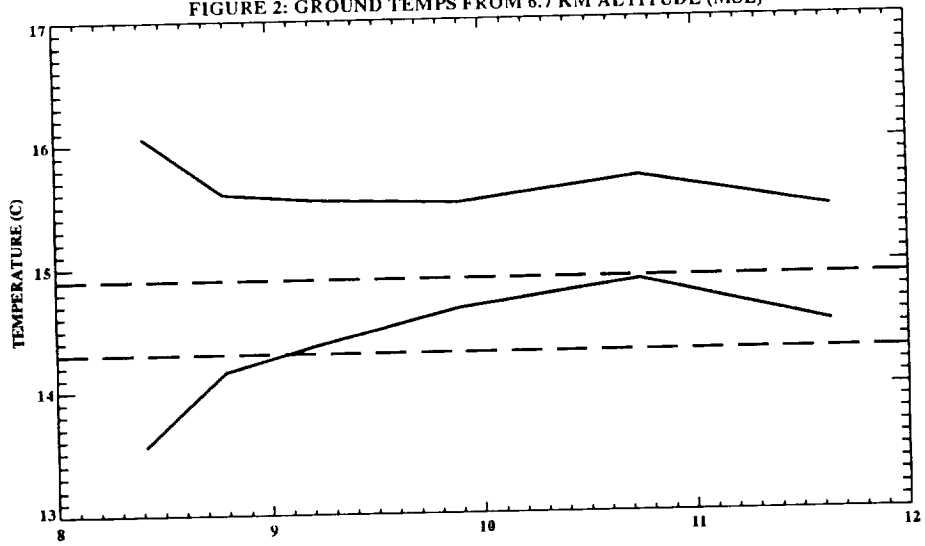
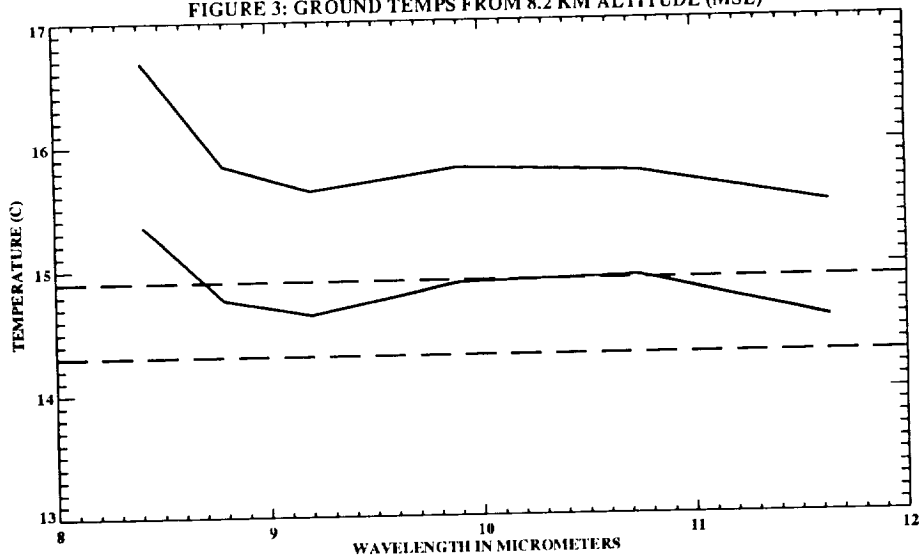


FIGURE 3: GROUND TEMPS FROM 8.2 KM ALTITUDE (MSL)



DISCRIMINATION OF ALKALINITY IN GRANITOID ROCKS: A POTENTIAL TIMS APPLICATION

Steven W. Ruff

Department of Geology, Arizona State University
Tempe, Arizona 85287-1404

1. INTRODUCTION

In mineral exploration, the ability to distinguish and map petrochemical variations of magmatic rocks can be a useful reconnaissance tool (e.g., Keith, 1986). Alkalinity is one such petrochemical parameter and is used in the characterization of granitoid rocks. In quartz normative plutonic rocks, alkalinity is related to the composition and abundance of feldspars. Together with quartz abundance, knowledge of feldspar modes allows the classification of these igneous rocks according to the Streckeisen diagram (Streckeisen, 1976). Alternative classification schemes rely on whole rock geochemistry instead of mineral identification. The relative ease of obtaining whole rock analyses means that geochemical classifications tend to be favored in exploration geology. But the technique of thermal infrared spectroscopy of rocks yields information on mineralogy and is one that can be applied remotely. The goal of the current work then is to establish whether data from TIMS can be used to distinguish the mineralogical variations that relate to alkalinity.

An ideal opportunity to test this thesis arises from the work presented in a paper by DeWitt (1989). This paper contains the results of mapping and analysis of Proterozoic plutonic rocks in north-central Arizona. The map resulting from this work delineates plutons according to alkalinity in an effort to establish a trend or polarity in the regional magmatism. Also contained within this paper are brief descriptions of the mineralogy of half of the region's plutons. This combination of mineralogical and geochemical information was the rationale behind choosing this area as a site for TIMS over flights. A portion of the region centered on the northern Bradshaw Mountains was selected because it contains plutons of all three alkalinity classifications (alkali-calcic, calc-alkalic, and calcic) present on DeWitt's map within a relatively small area (Figure 1). The site was flown in August of 1994 and the data received a few days before the writing of this manuscript. Most of this paper is devoted to the description of laboratory based spectroscopy and spectral simulations. These are required to gain insight into the correct procedures for enhancing the relatively small differences in the low spectral resolution TIMS data. Details of the TIMS analysis will be given at the presentation of this paper during the Workshop.

2. EXPERIMENTAL

High spectral resolution thermal emission data for the current work were acquired using a Mattson spectrometer at the Thermal Emission Spectrometer Laboratory of Arizona State University. A suite of minerals was selected that represents the major minerals described in the DeWitt paper. These include: the plagioclase feldspars albite through anorthite; the alkali feldspars microcline, orthoclase, and anorthoclase; the mafic minerals hornblende and biotite; and quartz. The purity of these mineral samples has been verified using microprobe analysis. All samples were particulate in form with a grain size of approximately 1mm. Emissivity spectra were calibrated using the technique of Ruff et al. (in preparation).

Mineral spectra were mixed synthetically using a computer. The linear mixing of spectral endmembers has been shown to be a valid technique by Thomson and Salisbury (1993). By mixing together in different proportions the spectra of the mineral suite, synthetic versions of granitoid rocks have been created. Because the mineralogy descriptions of the rocks in the DeWitt paper were presented without actual abundances (minerals were listed simply in order of decreasing abundance), all synthetic rock spectra are approximations. Textbook mineral modes (Ehlers and Blatt, 1982) were used to formulate the synthetic rock spectra.

To guide the choices necessary for TIMS data enhancement, TIMS channel bandwidths have been overlaid on all spectral plots. From the analysis of these plots, a strategy for image processing has been devised.

3. RESULTS

Figures 2 and 3 present individual mineral spectra. The feldspar spectra of Figure 2 are given in order of decreasing alkalinity from top to bottom and are displayed without normalization (i.e., depth of absorptions are accurate). As a group, the feldspars share many of the same spectral features as would be expected from crystal structure considerations. But upon closer inspection, a distinguishing trend can be noted. The shoulder present in the region of TIMS band 5 transitions to an absorption feature with decreasing alkalinity. This becomes especially apparent when compared with the emissivity of each mineral in the region of band 4.

In Figure 3, the remaining mineral spectra are plotted. These are also displayed without normalization but a scale change has been used to accommodate the deeper features. The depth of the biotite features is exaggerated because of the difficulty in obtaining a particulate sample with randomly oriented grains. In effect, the spectrometer is viewing only one side of the crystal, yielding a spectrum which is not representative of biotite in nature. For this reason, biotite has not been included in the synthetic mixtures.

The next plot depicts synthetically generated granitoid spectra. Figure 4 shows the spectral appearance of a generic granite, granodiorite, and tonalite which represent the three alkalinity classifications alkali-calcic, calc-alkalic, and calcic. Quartz and hornblende abundances are held constant in the mixtures at 25% and 10% respectively. The 65% total feldspar abundance is varied by composition to arrive at the three different rock types. The granite uses equal parts microcline and oligoclase. The more calcic granodiorite has andesine and labradorite in equal amounts. Finally, the tonalite contains the Ca-rich feldspars bytownite and anorthite.

As seen in the single mineral spectra, alkalinity discrimination is best observed in TIMS bands 4 and 5. The appearance of the band 5 feature as well as the decreased spectral contrast of the calcic plagioclases actually enhances the distinctive behavior of the rock spectra in bands 4 and 5.

4. DISCUSSION AND CONCLUSION

Based on the results of this work, it is theoretically possible for TIMS data to be used to discriminate between granitoid rocks of varying alkalinity. A ratio of bands 5 and 4 will yield values that can be used to enhance this discrimination. Using the technique of synthetically mixed rock spectra, many variations of mineral endmembers can be combined to determine whether the 5/4 ratio will persist as an alkalinity discriminator. With additional laboratory spectroscopy work and characterization of real samples, it may be found that the value of this ratio is unique and diagnostic of alkalinity.

The TIMS data from the Bradshaw Mountains site will be processed using the knowledge gained from this work. The map generated from the work of DeWitt will be compared to the processed TIMS images. At this time the effect of vegetation, rock coatings, weathering, and other real world variables has not been examined. Whether these factors completely confound the promising results seen in the lab is to be determined.

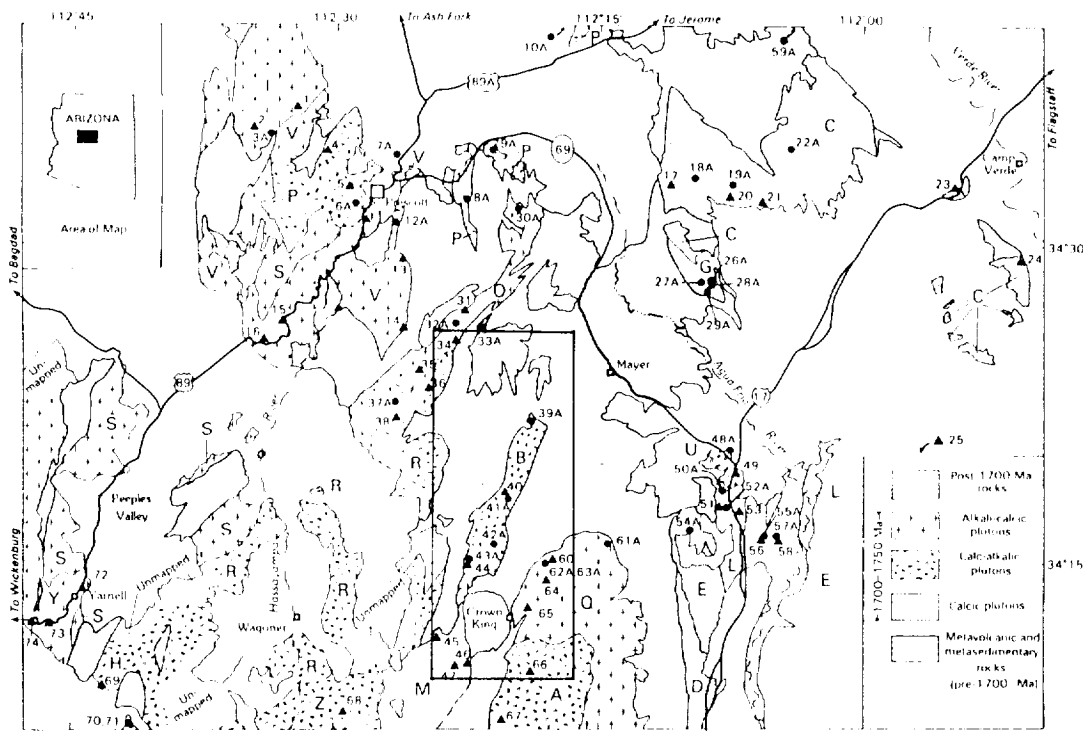
5. ACKNOWLEDGMENTS

I would like to thank the crew of the NASA C-130 for allowing me and the rest of the ASU group to fly along during the TIMS missions. We were treated like VIP's and encouraged to participate in planning. It was a rewarding and enjoyable experience.

6. REFERENCES

- DeWitt, E., 1989, "Geochemistry and tectonic polarity of early proterozoic (1700-1750-Ma) plutonic rocks, north-central Arizona," in Jenney, J. P. and Reynolds, S. J., *Geologic Evolution of Arizona*, Ariz. Geol. Soc. Digest, vol. 17, pp. 149-163.
- Ehlers, E.G., and H. Blatt, 1982, *Petrology*, W.H. Freeman and Company, San Francisco, pp. 100-113.
- Keith, S.B., 1986, "Petrochemical variations in Laramide magmatism and their relationships to Laramide tectonic and metallogenic evolution in Arizona and adjacent regions" in Beatty, Barbara and P.A.K. Wilkinson eds., *Frontiers in geology and ore deposits of Arizona and the Southwest: Tucson, Ariz.* Geol. Soc. Digest, vol. 16, pp. 89-101.
- Streckeisen, A., 1976, "To each plutonic rock its proper name," *Earth Sci. Rev.*, vol.12, pp. 1-33.
- Strong, D. F., 1988, "A review and model for granite-related mineral deposits," in Taylor, R. P. and D.F. Strong, eds., *Recent Advances in the Geology of Granite-Related Mineral Deposits. Can. Inst. Mining and Metall. Spec.*, vol. 39, pp. 424-45.
- Thomson, J. L. and J.W. Salisbury, 1993, "The mid-infrared reflectance of mineral mixtures (7-14 μm)," *Rem. Sens. Env.*, vol 45, pp. 1-13.

Figure 1. Simplified geologic map of the Prescott area, north-central Arizona (from DeWitt, 1989).



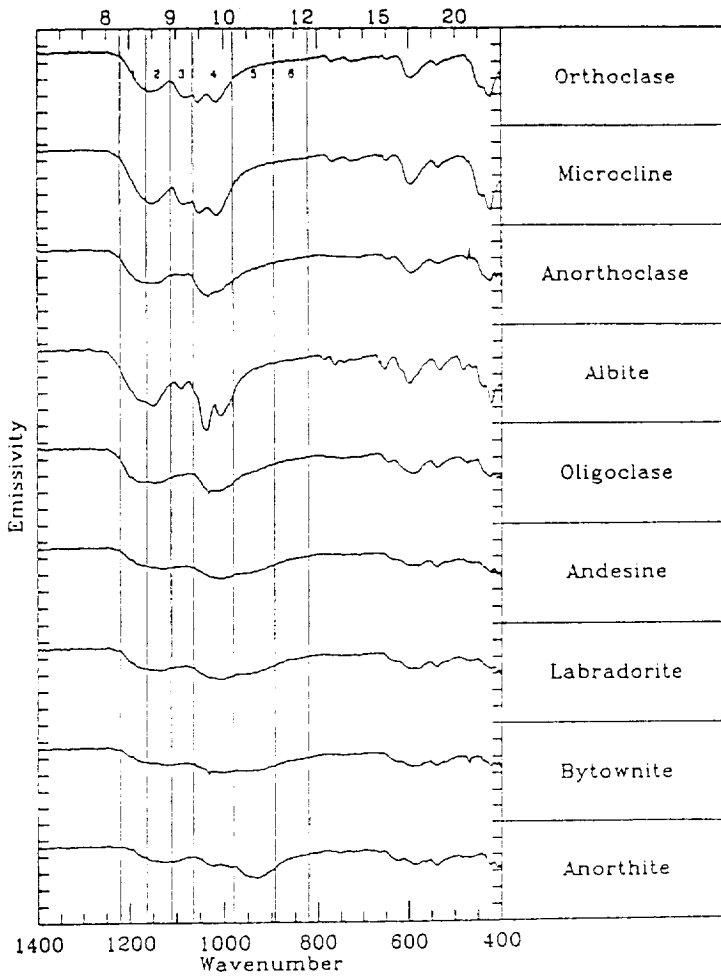


Figure 2. Spectra of feldspar suite.

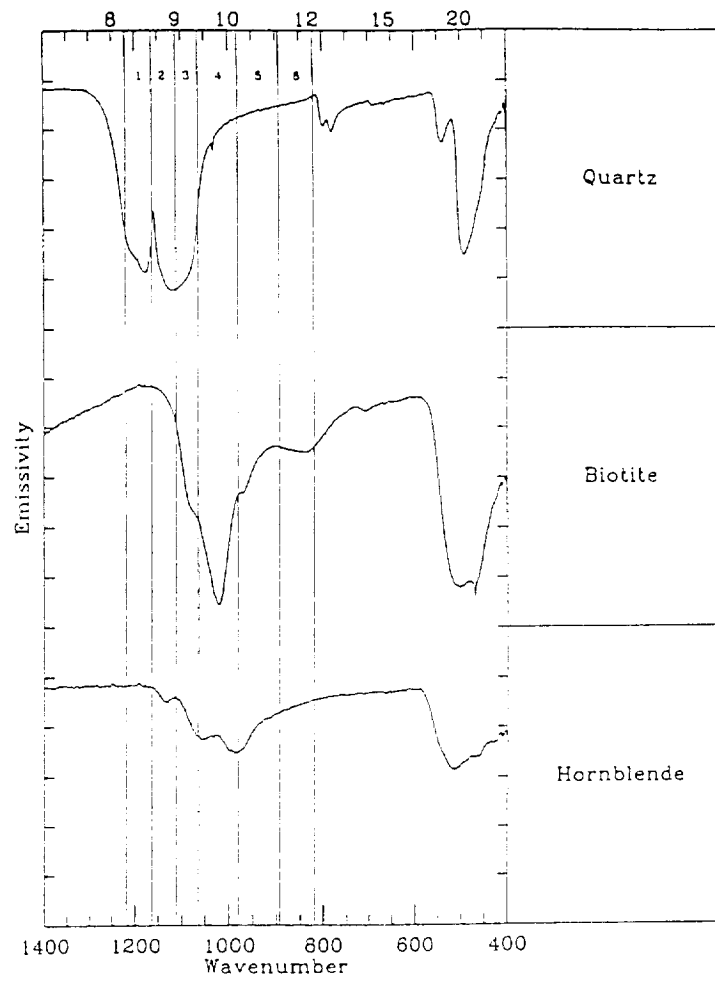


Figure 3. Additional granitoid suite mineral spectra.

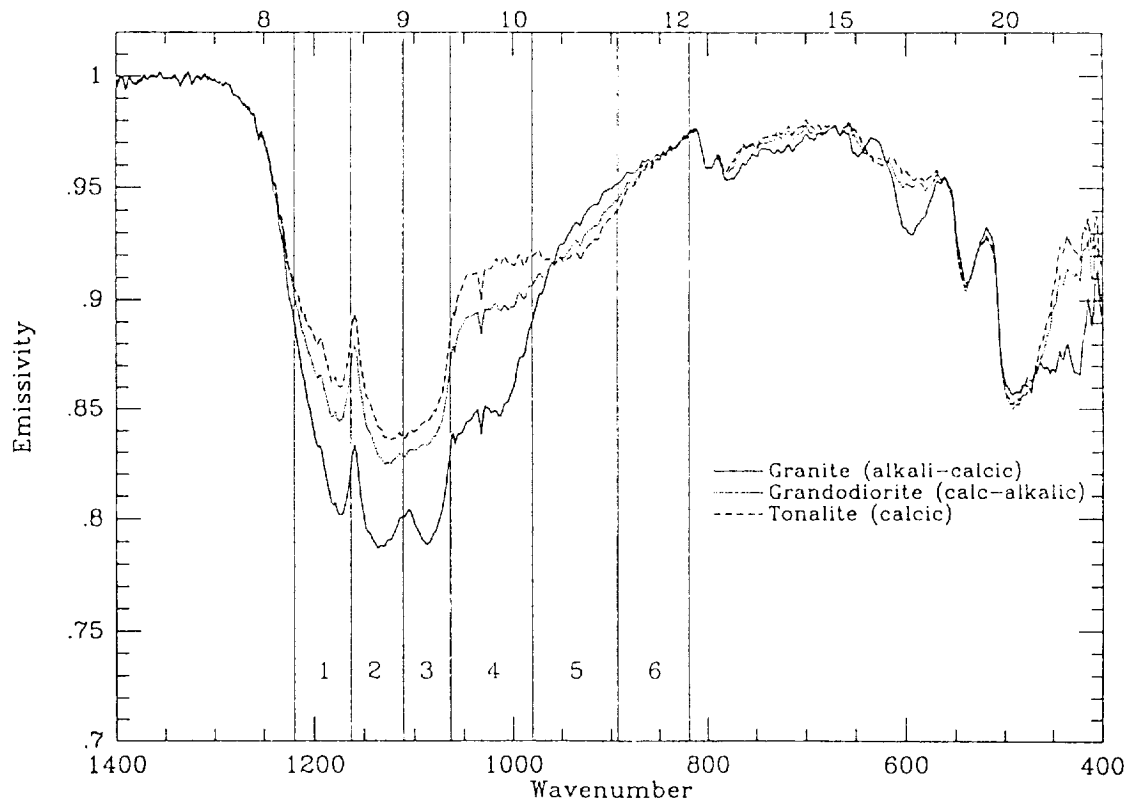


Figure 4. Synthetic rock spectra.

TIMS OBSERVATIONS OF SURFACE EMISSIVITY IN HAPEX-SAHEL

Thomas Schmugge
USDA Hydrology Lab, Beltsville, MD, 20705

Simon Hook and Anne Kahle
Jet Propulsion Laboratory, California Institute of Technology
Pasadena, CA, 91109

1. INTRODUCTION

The Thermal Infrared Multispectral Scanner (TIMS) was flown on the NASA C-130 aircraft for a series of 12 flights during HAPEX-Sahel at altitudes ranging from 0.25 to 6 km (0.6 to 15 m resolution). TIMS provides coverage of the 8 to 12 micrometer thermal infrared band in 6 contiguous channels. Thus it is possible to observe the spectral behavior of the surface emissivity over this wavelength interval.

2. DISCUSSION

A high resolution image, 1.5 m, of the west central site on 2 September 1992 was processed and the spectral behaviors of the millet and fallow grassland sites were determined. There was a 4 to 5 K difference in the brightness temperature over the 6 channels when significant bare soil was visible. Channels 1 to 3 (8.2 to 9.6 micrometers) were 4-5 K cooler than the longer wavelength channels which is characteristic of soils rich in quartz. These differences in brightness were converted to emissivity differences using both the emissivity normalization and alpha residuals methods. Both methods yielded about the same difference in emissivity over the 6 channels, i.e. 0.09. However the alpha residuals methods yielded higher absolute values. As expected for a group of vegetated pixels, there was little difference in emissivity, less than 0.02 over the 6 channels, and the average was about 0.99. The extracted vegetation temperature was close to the air temperature, while for the bare soil it was at least 10 K higher.

ACKNOWLEDGMENT

A portion of the research described in this paper was performed at the Jet Propulsion Laboratory, California Institute of Technology, under a contract with the National Aeronautics and Space Administration.

Reference herein to any specific commercial product, process, or service by trade names, trademark, manufacturer or otherwise does not imply endorsement by the United States or the Jet Propulsion Laboratory, California Institute of Technology.



A FIELD- AND LABORATORY-BASED QUANTITATIVE ANALYSIS OF ALLUVIUM: RELATING ANALYTICAL RESULTS TO TIMS DATA

Melissa L. Wenrich, Victoria E. Hamilton, and Philip R. Christensen

Department of Geology, Arizona State University
Tempe, Arizona 85287-1404

1. INTRODUCTION

Thermal Infrared Multispectral Scanner (TIMS) data were acquired over the McDowell Mountains northeast of Scottsdale, Arizona during August 1994. The raw data were processed to emphasize lithologic differences using a decorrelation stretch and assigning bands 5, 3, and 1 to red, green, and blue, respectively (Gillespie et al., 1986). Processed data of alluvium flanking the mountains exhibit moderate color variation. The objective of this study was to determine, using a quantitative approach, what environmental variable(s), in the absence of bedrock, are responsible for influencing the spectral properties of the desert alluvial surface.

2. ANALYTICAL METHODS AND RESULTS

2.1 FIELD

To quantify the surface properties of the alluvium, two linear field traverses were defined along which data were collected at individual points and appropriately averaged. By averaging the data, the effect of small-scale surface variability is removed, thus the data better reflect the overall character of the surface. The positions of the transects were defined to cross alluvial surfaces displaying the maximum color variation in the TIMS image. The boundaries of the adjacent distinctly colored areas are washes, as verified during fieldwork. Large-scale vegetation such as creosote, palo verde, saguaro, and low scrub constitutes 10-15% of the surface area surrounding the transects. Because this value applies to both transect locations, macro-vegetation was ruled out as a controlling factor for the variation in the TIMS data. At twenty-foot intervals along the transects, three-foot square sample sites were examined and rock samples were collected for laboratory spectral analysis. Prior to sample collection at each site, the areal percentage of soil and the percentage of each rock type were quantified (Figures 1 and 2). The average percentage of soil over the entire length of transects 1 and 2 (ignoring the data points within washes) is 11.8% and 0.8%, respectively. When sample points within a given color unit are averaged, the soil percentage deviates from the average by a maximum of 2.9% (transect 1) and 0.6% (transect 2); these values are too small to account for the image color variation along each transect. Two dominant rock types were identified as various quartzites and phyllitic schists. Figures 2a and 2b display the systematic variation in rock type percentage along each transect. Transect 1 is segmented by two washes and transect 2 is segmented by one wash. For each transect segment the average percentage of rock compositions was calculated. From the first segment (A) to the last segment (C) of transect 1, the percentage of quartzite increases from 20.6% to 66.1% as the percentage of phyllitic schist decreases from 58.6% to 19.1%. A similar trend occurs along transect 2, along which the percentage of quartzite increases from 1.4% to 70.2% as the percentage of phyllitic schist decreases from 97.8% to 26.8%. The shifts in dominant mineralogy correlate well to the areas defined by the TIMS colors, suggesting that the rock composition of the surface alluvium determines the TIMS spectral signature and swamps the effects of vegetation or soil.

2.2 LABORATORY

Thermal infrared spectra of nineteen rock samples were acquired in emission over the range of 1400 to 450 cm^{-1} (~ 7 to $22\ \mu\text{m}$) using a modified Mattson Cygnus 100 interferometer/spectrometer. These vibrational spectra were separated into two groups based on the most apparent distinction which is overall absorption feature depth. Subsequently, these two groups were found to correspond to the two general rock types identified in the field. The nine quartzite and eleven schist laboratory spectra were averaged to produce a representative endmember spectrum for each rock group; the resulting quartzite and phyllitic schist spectra are shown in Figure 3. The spectrum of the average quartzite exhibits deep absorptions at frequencies similar to those of quartz, suggesting a quartz composition with minor impurities. The spectral positions and shapes of the average phyllitic schist absorptions suggest that the schists are silicic and similar to the quartzites; however, the absorptions are 45% shallower than the quartzite features and the schist spectrum exhibits an additional feature within the TIMS wavelength range at 1040 cm^{-1} ($9.6\ \mu\text{m}$) which was determined by normalizing the two average endmember quartzite and phyllite spectra over the range of 770 to 750 cm^{-1} (~ 13.0 to $13.3\ \mu\text{m}$) and differencing them. The difference spectrum (Figure 3) is indicative of clay mineralogy. No further spectral analysis was performed to identify the specific type of clay. The compositional dissimilarity between the schists and the quartzites provides the basis for distinguishing the alluvial surfaces in the TIMS data. The overall spectral similarity of the rock samples prompted thin section preparation and compositional analysis to verify the presence of clay in the phyllitic schists. We anticipate results of thin section analysis by the time of the conference.

3. CORRELATION OF TIMS DATA WITH FIELD AND LABORATORY RESULTS

3.1 PROCEDURE

Spectral endmembers derived from TIMS image

Quartzite and phyllitic schist endmember compositions of the alluvial rock suite (Figure 4) were selected from the digital TIMS image using the bedrock compositions nearest the transects. We have assumed that the primary sources of the alluvial materials are proximal because the rock fragments are angular. To evaluate the method of mixing endmember spectra derived from TIMS data and determine accurate areal percentages of mixed pixels, endmember spectra derived from the TIMS image were linearly summed according to Ramsey and Christensen [1992] using the average percentage of quartzite and phyllitic schist observed for each distinctly colored area along the transects. The resultant mixed spectra were then compared to spectra averaged over 4 by 4 pixel squares for each distinct color area in the TIMS image along the transects.

The mixed spectra derived from the TIMS endmembers have emissivities that plot within 2% of the spectral emissivities derived directly from the transect segments in the TIMS image. This degree of accuracy suggests that the rock percentages were correctly quantified in the field.

Spectral endmembers derived from laboratory analysis

Laboratory spectra were linearly mixed [Ramsey and Christensen, 1992] according to the average rock percentages observed for each segment along the transects. Because the laboratory spectra were acquired at 4 cm^{-1} resolution, the mixed spectra were deconvolved to TIMS resolution (Figure 5).

Subsequent comparison of the lab spectra with TIMS spectra of the same alluvial areas shows two primary differences. Firstly, the emissivities of the TIMS spectra are greater than .96, whereas the laboratory spectral emissivities are as low as .72. Secondly, quartzite-dominated spectra in both data sets exhibit a distinct quartz absorption feature in band 3; however bands 1, 5, and 6 in the TIMS data show additional absorptions not present in the laboratory spectra. We believe these additional TIMS features do not result from vegetation (assuming unit emissivity) but may be due to absorptions from a soil component which was not included as a laboratory endmember.

4. CONCLUSIONS

In order to determine the effects of vegetation, soil, and rock mineralogy on the thermal emission spectral properties of two alluvial surfaces flanking the McDowell Mountains, AZ, a quantitative survey of the areal extent of these environmental variables was conducted. Our study suggests that vegetation and soil do not strongly affect the TIMS image and that the composition of rock fragments is the primary control on the spectral signature. The two main lithologies present along the field transects are quartzites and phyllitic schists derived from separate upslope bedrock sources. Effective mixing of these lithologies is inhibited by washes that intersect the transects and act as natural barriers to talus migration. Washes in the field area correlate with the boundaries of the various colored areas in the TIMS data confirming that mixing is inhibited and that TIMS color differences result from dominant rock type. Mixing TIMS-derived endmember (bedrock) spectra according to the average percentage of each rock type for the five transect segments produced spectral emissivities which lie within 2% of the emissivities derived from the same transect areas in the TIMS image.

NOTE: A color slide of the processed TIMS data of the field area may be obtained from the authors by request.

5. ACKNOWLEDGEMENT

We would like to thank the Ames Research Center C-130 crew for allowing us to participate in the overflights. We greatly appreciate being so closely involved during the data collection.

6. REFERENCES

- Gillespie, A.R., A.B. Kahle, and R. Walker, 1986, "Color enhancement of highly correlated images: I. Decorrelation and HSI contrast stretches", *Remote Sensing Environ.*, vol. 20, pp. 209-235.
- Ramsey, M.S. and P.R. Christensen, 1992. "Ejecta patterns of Meteor Crater, Arizona derived from the linear un-mixing of TIMS data and laboratory thermal emission spectra", in *Proc. of the Third TIMS Workshop*: Abbott, E.A., ed., JPL Publ. 92-14, JPL, Pasadena, Calif., pp. 34-36.

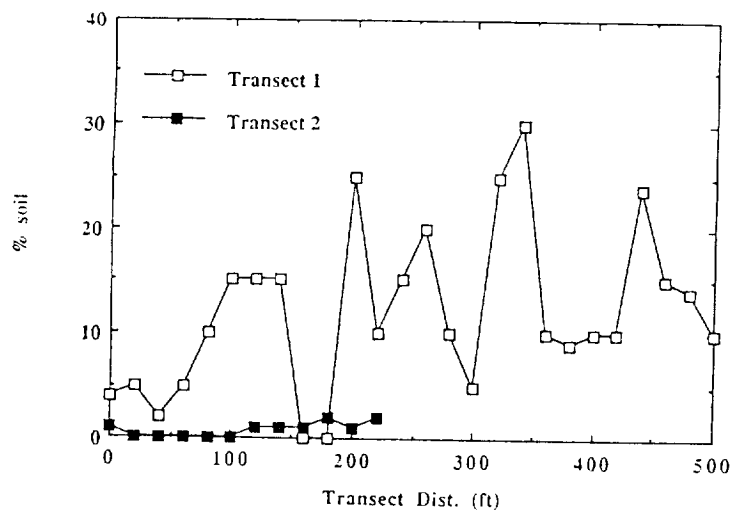


Figure 1. Areal percentage of soil at each sample site along transects 1 and 2.

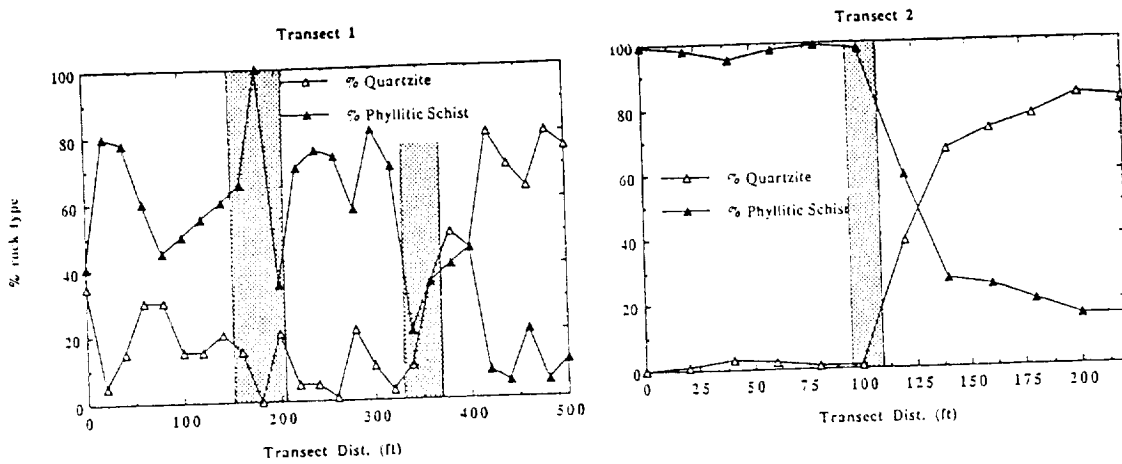


Figure 2. Areal percentage of rock type at each sample site along transect 1 (a) and transect 2 (b). Stippled areas represent data points acquired in washes.

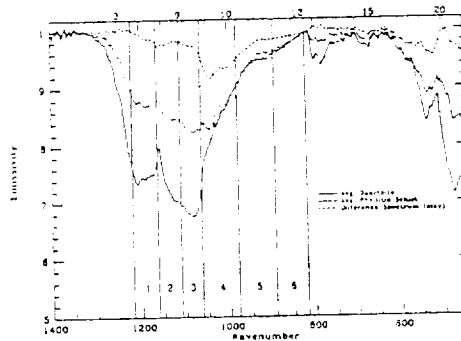


Figure 3. Averaged laboratory quartzite, phyllitic schist, and differenced clay spectra. Tims bands are labeled 1-6.

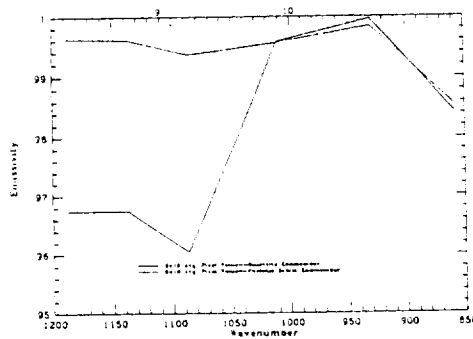


Figure 4. Quartzite and phyllitic schist endmember spectra derived from Tims data. Bedrock proximal to the transects was used.

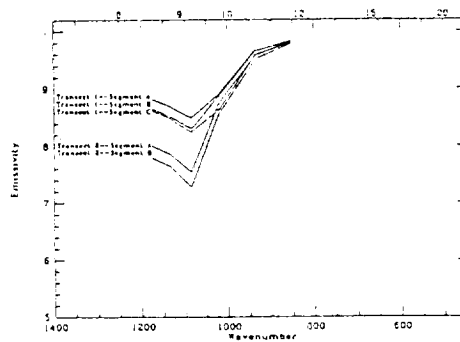


Figure 5. Mixed laboratory spectra deconvolved to Tims resolution.

1. Report No. 95-1, Vol. 2		2. Government Accession No.		3. Recipient's Catalog No.	
4. Title and Subtitle Summaries of the Fifth Annual JPL Airborne Earth Science Workshop, January 23-26, 1995, Vol. 1: AVIRIS Workshop				5. Report Date January 23, 1995	
7. Author(s) Robert O. Green (editor)				6. Performing Organization Code	
9. Performing Organization Name and Address JET PROPULSION LABORATORY California Institute of Technology 4800 Oak Grove Drive Pasadena, California 91109				8. Performing Organization Report No.	
12. Sponsoring Agency Name and Address NATIONAL AERONAUTICS AND SPACE ADMINISTRATION Washington, D.C. 20546				10. Work Unit No.	
				11. Contract or Grant No. NAS7-1260	
				13. Type of Report and Period Covered JPL Publication	
				14. Sponsoring Agency Code RF 4 BP-665-81-00-00-00	
15. Supplementary Notes					
16. Abstract This publication contains the summaries for the Fifth Annual JPL Airborne Earth Science Workshop, held in Pasadena, California, on January 23-26, 1995. The main workshop is divided into three smaller workshops as follows: o The Airborne Visible/Infrared Imaging Spectrometer (AVIRIS) workshop, on January 23-24. The summaries for this workshop appear in Volume 1. o The Airborne Synthetic Aperture Radar (AIRSAR) workshop, on January 25-26. The summaries for this workshop appear in Volume 3. o The Thermal Infrared Multispectral Scanner (TIMS) workshop, on January 26. The summaries for this workshop appear in Volume 2.					
17. Key Words (Selected by Author(s)) 1. Geosciences and Oceanography (General) 2. Geology and Mineralogy 3. Hydrology and Limnology 4. Infrared and Ultraviolet Detection			18. Distribution Statement Unclassified; unlimited		
19. Security Classif. (of this report) Unclassified		20. Security Classif. (of this page) Unclassified		21. No. of Pages 172	22. Price

